Resource

Cell Chemical Biology

# Discovery of Protein-Protein Interaction Inhibitors by Integrating Protein Engineering and Chemical Screening Platforms

## Graphical Abstract

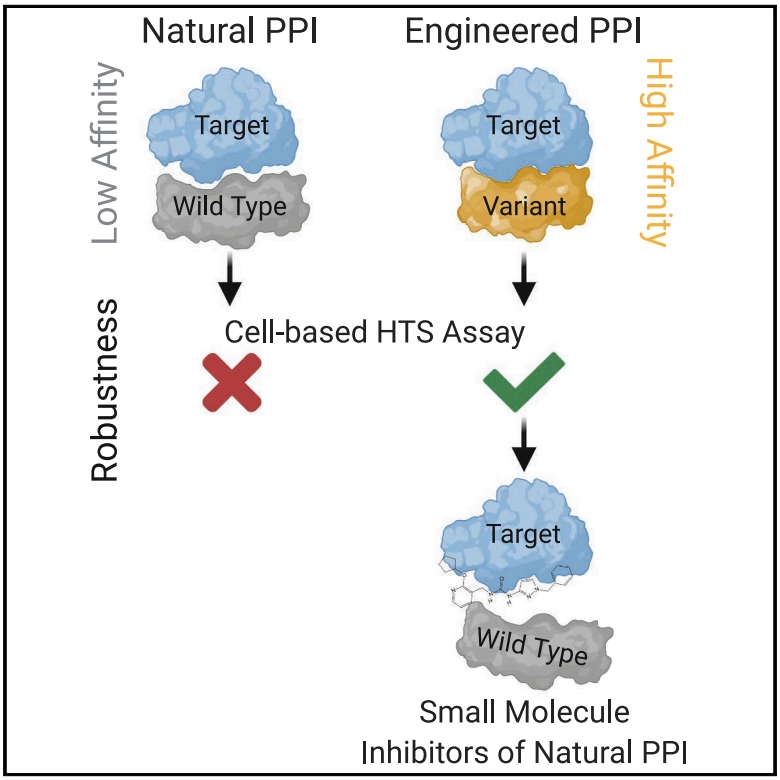


## Highlights

- Variants enable generation of robust cell-based assays and enable HTS
- Identified small molecules directly bind to the NEMO target protein
- Validated top chemical hits inhibit endogenous NF-κB signaling in cells

## Authors

Timurs Maculins, Javier Garcia-Pardo, Anamarija Skenderovic, ..., Volker Dötsch, Masato Akutsu, Ivan Dikic

## Correspondence

maculins.timurs@gene.com (T.M.), dikic@biochem2.uni-frankfurt.de (I.D.)

## In Brief

Maculins et al. describe an approach for identifying small molecule inhibitors of protein-protein interactions that are considered "hard to target." The team engineered high-affinity variants of one interacting partner that enabled robust chemical screening. Top hits identified using this approach inhibited cellular signaling driven by the endogenous interaction.

Maculins et al., 2020, Cell Chemical Biology *27*, 1441–1451
November 19, 2020 
https://doi.org/10.1016/j.chembiol.2020.07.010

CellPress

Cell Chemical Biology

CellPress

Resource

# Discovery of Protein-Protein Interaction Inhibitors by Integrating Protein Engineering and Chemical Screening Platforms

Timurs Maculins,[1,2,9,*] Javier Garcia-Pardo,[1,2,3] Anamarija Skenderovic,[3] Jakob Gebel,[4] Mateusz Putyrski,[1,2] Andrew Vorobyov,[2] Philipp Busse,[1,3] Gabor Varga,[1,2] Maria Kuzikov,[5] Andrea Zaliani,[5] Simin Rahighi,[8] Veronique Schaeffer,[1] Michael J. Parnham,[2] Sachdev S. Sidhu,[6,7] Andreas Ernst,[1,2] Volker Dötsch,[4] Masato Akutsu,[3] and Ivan Dikic[1,2,3,10,*]

[1]Institute of Biochemistry II, Goethe University, Frankfurt am Main, Germany
[2]Fraunhofer Institute for Molecular Biology and Applied Ecology IME, Branch for Translational Medicine and Pharmacology, Theodor-Stern-Kai 7, 60596 Frankfurt am Main, Germany
[3]Buchmann Institute for Molecular Life Sciences, Frankfurt am Main, Germany
[4]Institute of Biophysical Chemistry & Center for Biomolecular Magnetic Resonance, Goethe University, Max-von-Laue-Strasse 9, 60438 Frankfurt am Main, Germany
[5]Fraunhofer Institute for Molecular Biology and Applied Ecology Screening Port, Hamburg, Germany
[6]The Donnelly Centre, University of Toronto, Toronto, ON M5S 3E1, Canada
[7]Department of Molecular Genetics, University of Toronto, Toronto, ON M5S 1A8, Canada
[8]Chapman University School of Pharmacy (CUSP), Harry and Diane Rinker Health Science Campus, Chapman University, Irvine, CA 92618, USA
[9]Present address: Department of Cancer Immunology, Genentech Inc., South San Francisco, CA, USA
[10]Lead Contact
*Correspondence: maculins.timurs@gene.com (T.M.), dikic@biochem2.uni-frankfurt.de (I.D.)
https://doi.org/10.1016/j.chembiol.2020.07.010

## SUMMARY

Protein-protein interactions (PPIs) govern intracellular life, and identification of PPI inhibitors is challenging. Roadblocks in assay development stemming from weak binding affinities of natural PPIs impede progress in this field. We postulated that enhancing binding affinity of natural PPIs via protein engineering will aid assay development and hit discovery. This proof-of-principle study targets PPI between linear ubiquitin chains and NEMO UBAN domain, which activates NF-κB signaling. Using phage display, we generated ubiquitin variants that bind to the functional UBAN epitope with high affinity, act as competitive inhibitors, and structurally maintain the existing PPI interface. When utilized in assay development, variants enable generation of robust cell-based assays for chemical screening. Top compounds identified using this approach directly bind to UBAN and dampen NF-κB signaling. This study illustrates advantages of integrating protein engineering and chemical screening in hit identification, a development that we anticipate will have wide application in drug discovery.

## INTRODUCTION

Protein-protein interactions (PPIs) play pivotal roles in biological processes (Stumpf et al., 2008). In protein interaction networks, many PPIs are transient, established via an upstream signaling event or regulated by post-translational modifications (PTMs) (Perkins et al., 2010). Mutations or impaired regulation of PPIs affect cellular networks and contribute to disease development. The discovery of PPI inhibitors with the intention to modulate aberrant pathways has therefore attracted considerable interest from the pharmaceutical industry (Arkin et al., 2014). Small molecules are ideally suited as PPI inhibitors due to their ability to access PPI interfaces, ease of administration, and good bioavailability. Therefore, approaches to modulate PPIs with small molecules resulted in the development of new forms of therapy (Arkin et al., 2014). However, there are a number of challenges associated with the development of small-molecule PPI inhibitors that have prevented the field from reaching its full potential (Laraia et al., 2015). One such limitation is inherently weak binding affinity between interacting protein partners, which often hinders the development of robust high-throughput screening (HTS) assays. This is particularly relevant in the context of cell-based assays that translate affinity interaction within the cellular milieu into a readout, the robustness of which is a determining factor for the outcome of screening campaigns.

The functional importance of PPIs and the associated regulatory mechanisms is clearly illustrated in the nuclear factor κB (NF-κB) pathway, which controls cellular inflammatory and

immune responses and is governed by different PTMs. As one of the most diverse PTM forms, ubiquitylation modulates the NF-κB signaling pathway at multiple levels (Popovic et al., 2014). The biological consequence of protein ubiquitylation is triggered via the recognition of ubiquitin (Ub) or Ub chains by linkage-specific Ub-binding domains, therefore inducing the desired cellular response (Husnjak and Dikic, 2012; Komander and Rape, 2012). The linkage-specific interaction between the Ub binding in ABIN proteins and NEMO (UBAN) domain of the NF-κB essential modulator (NEMO) and head-to-tail linked linear Ub chains triggers NF-κB activation (Haas et al., 2009; Tokunaga et al., 2009). This PPI is characterized by a relatively low binding affinity with a dissociation constant ($K_D$) in the low-micromolar range, suggesting that it can be easily formed or broken depending on the upstream dynamic regulation of the NF-κB pathway (Lo et al., 2009; Rahighi et al., 2009). Once formed, this PPI drives the activation of I-κB kinase (IKK), which is essential for the nuclear translocation of NF-κB transcription factor family members and the regulation of immune and inflammatory signaling processes (Iwai and Tokunaga, 2009).

Dysregulation of the NF-κB pathway is associated with multiple diseases, including tumorigenesis and inflammatory disorders. This has prompted concerted efforts by the pharmaceutical industry and academia to develop inhibitors against NF-κB activation (Taniguchi and Karin, 2018). Several tumor necrosis factor (TNF), interleukin-1 (IL-1) and IL-6 receptor antagonists, and JAK inhibitors are approved for use in the clinic as therapies that antagonize the NF-κB pathway. Additionally, vast drug-discovery efforts have led to the identification of numerous small-molecule inhibitors of the IKK β-kinase subunit (IKKβ) as the ubiquitous signal integration hub for NF-κB activation. However, these molecules have severe on-target toxicities and as such have not been approved for use as therapeutics (Llona-Minguez et al., 2013).

In a search for alternative therapeutic strategies, more attention has been drawn to the linear ubiquitin chain assembly complex (LUBAC), which generates linear Ub chains and is associated with activated B cell-like subtype of diffuse large B cell lymphoma (ABC-DLBCL) and resistance to chemotherapy in lung cancer (Ruiz et al., 2019; Yang et al., 2014). Recent approaches have identified LUBAC inhibitors that reduce the generation of linear Ub chains and dampen NF-κB pathway activation, representing potential lead molecules for further development (Johansson et al., 2019; Katsuya et al., 2019; Sakamoto et al., 2015). Additionally, the specific interaction between UBAN and linear Ub chains represents an alternative strategy toward attenuating the activation of the NF-κB pathway. This PPI involves the UBAN Ub-binding epitope and the canonical hydrophobic patch of the distal Ub, supported by proximal Ub surface in the linear Ub chain (Lo et al., 2009; Rahighi et al., 2009). This interaction has a relatively low binding affinity; however, an *in vitro* biochemical screening approach validated that this PPI as being susceptible to small-molecule inhibition (Vincendeau et al., 2016). While this is promising, to date no cell-based assays have been established to look at the inhibition of this PPI and the associated functional consequences in a physiological setting. As a weak binding affinity between interaction partners often hampers the development of such assays, we envisioned that the use of protein engineering to enhance the binding affinity between the UBAN domain of NEMO and Ub might aid assay development, thereby facilitating hit discovery.

To explore this, we employed a combinatorial, phage-displayed library of Ub variants (Ubvs) that encodes mutations at residue positions that are engaged in binding to the UBAN domain of NEMO (Ernst et al., 2013). Using phage display, we identified monomeric Ubv-A that binds UBAN with ~9-fold improved binding affinity compared with linear Ub chains. We show that Ubv-A acts as a competitive inhibitor of linear Ub chain binding to UBAN and attenuates NF-κB activation in cells. Importantly, the UBAN:Ubv-A crystal structure revealed that Ubv-A binds the same epitope on UBAN that is used for binding to linear Ub chains. Therefore, we proposed that employing this high-affinity interaction in a cell-based HTS platform might lead to the identification of small molecules that act via binding to UBAN. To test this, we designed a cell-based assay that exploits the complementation of split nanoluciferase as a readout for UBAN and Ubv-A binding. Interrogation of a chemical library enriched with compounds that harbor PPI inhibitor qualities resulted in the identification of a subset of hits that are active in the assay, bind to the UBAN domain of NEMO, and attenuate NF-κB nuclear translocation in cells. Together, this outlines the added benefits of utilizing engineered high-affinity protein variants as tools in chemical screening to facilitate hit discovery.

## RESULTS

### Generation of High-Affinity Ubv Binders to the UBAN Domain of NEMO

The PPI between the UBAN domain of NEMO and linear dimeric ubiquitin (2xUb) chains is of low affinity, with a $K_D$ of 3.2 μM (Figure S1A). This PPI is mediated by the linear linkage between Ub molecules, as $K_D$ of UBAN with 2xUb chains linked via lysine (K) 63, K48, or monomeric Ub (1xUb) in our assay could not be determined due to their extremely low affinities (Figures S1B–S1D). To leverage the advantages of cell-based screening, we attempted to develop an assay to read out the interaction between ectopically expressed deubiquitinating enzyme (DUB)-resistant linear Ub chains, in which the terminal glycine residue is mutated to valine in each Ub monomer, and UBAN in cells. However, we were not successful in generating a robust assay readout that would be compatible with HTS (data not shown), presumably due to the very low binding affinity of this PPI. We therefore hypothesized that generating a variant of one interaction partner of this PPI, such as a variant that mimics linear Ub chain binding to UBAN, would enable robust assay development and an efficient HTS campaign.

We used phage display technology to generate high-affinity Ub variants (Ubvs) to the murine UBAN domain of NEMO (UBAN). We applied a soft randomization approach to generate the Ubv library by introducing mutations in the regions of Ub that are engaged in the interaction with UBAN in the context of linear Ub chains (named Regions 1, 2, and 3 in Figure 1A). Following phage selections, we isolated 23 unique Ubvs and determined their half-maximal inhibitory concentration ($IC_{50}$) by quantifying their binding to surface-immobilized UBAN while competing with set concentrations of free UBAN in solution using clonal phage enzyme-linked immunosorbent assay (ELISA) (Figure S1E). The best binder (Ubv-A) was selected for further

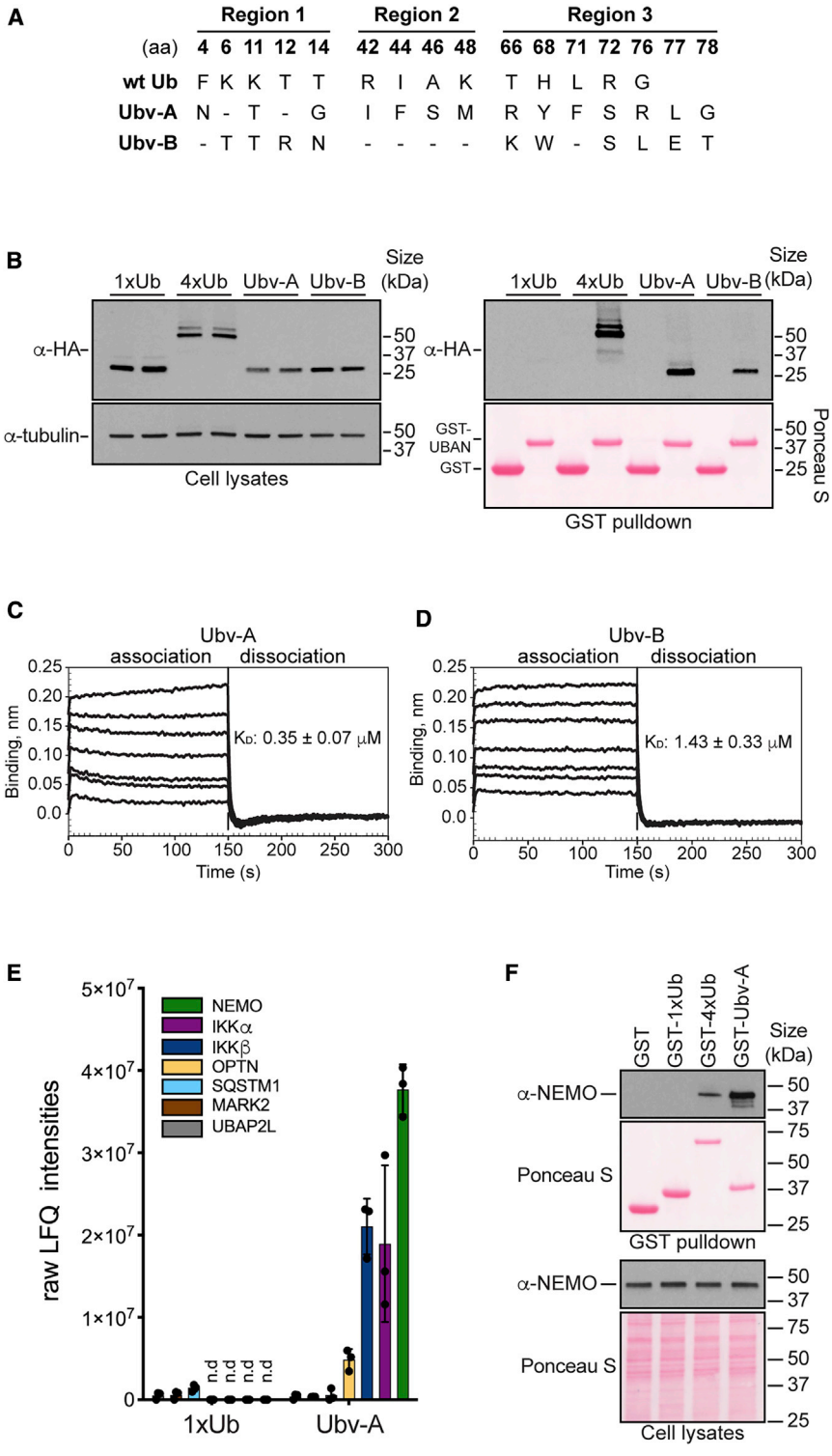


**Figure 1. Generation of High-Affinity Ubv Binders to the UBAN Domain of NEMO**

(A) The amino acid (aa) sequence alignment of wild-type ubiquitin (wt Ub), Ubv-A, and Ubv-B shows only those positions that were diversified in the Ub variant library, denoted as Regions 1, 2, and 3. Dashes indicate amino acids that were conserved as wild-type sequence. See also Figure S1E.

(B) A representative GST pull-down experiment using lysates of HEK293T cells transiently transfected with either hemagglutinin-tagged monomeric Ub in which the terminal glycine residue is mutated to valine (1xUb), tetrameric UbG76V fusion (4xUb), or monomeric Ubv-A or Ubv-B with beads conjugated to either GST or GST-UBAN (n = 3). Ponceau staining and α-tubulin western blot were used as loading controls.

(C and D) Representative biolayer interferometry (BLI) binding assay with immobilized GST-human UBAN and Ubv-A (C) or Ubv-B (D) added at 20, 10, 5, 2.5, 1.25, 0.625, or 0.3125 μM concentrations (n = 3, technical replicates). Dissociation constants ($K_D$) are indicated on the graphs. See also Figures S1A–S1D.

(E) Graph shows raw label-free quantification (LFQ) intensities of NEMO, IKKα and IKKβ, OPTN, and other ubiquitin binding domain-containing proteins identified in interactomes of the control UbG76V (1xUb) and Ubv-A IP-MS (n = 3, technical replicates). Data are presented as mean ± SD. See also Figure S1F.

(F) A representative GST pull-down experiment using lysates of HEK293T cells with beads conjugated to control GST or GST-1xUb, 4xUb, or Ubv-A (n = 3). See also Figures S1K–S1L for purity checks of GST fusions used in this study.

validation together with another high-affinity binder (Ubv-B) that lacks Region 2 mutations in the Ub hydrophobic patch (Figure 1A).

First, we tested whether Ubv-A and Ubv-B interact with UBAN in cell lysates. As expected, UBAN interacted with tetrameric linear Ub chains (4xUb) but not with 1xUb, since linear Ub linkage is required for this PPI. Importantly, similar to linear Ub chains, UBAN also pulled down monomeric Ubv-A and Ubv-B (Figure 1B). Next, we used biolayer interferometry (BLI) to determine binding affinities of Ubv-A and Ubv-B to UBAN, which were improved ~9-fold and ~2-fold when compared with linear 2xUb chains, with $K_D$ of 0.35 μM and 1.43 μM, respectively (Figures 1C and 1D). Based on these observations, we prioritized Ubv-A in this study.

The UBAN domain is highly conserved and is present in A20-binding inhibitor of NF-κB activation (ABIN) and Optineurin (OPTN) proteins (Wagner et al., 2008). To determine the specificity of Ubv-A binding to NEMO in cells, we performed immunoprecipitation coupled with mass spectrometry (IP-MS). NEMO, IKKα, and IKKβ subunits of the IKK complex were among the top interacting proteins that were enriched more than 2-fold in Ubv-A IP-MS when compared with 1xUb control (Figure S1F). OPTN was also present within the group of high-confidence interacting proteins; however, it displayed at least 6-fold reduced

enrichment compared with NEMO. Other Ub-binding domain-containing proteins present in the IP-MS dataset were not significantly enriched (Figure 1E). We further demonstrated that, as with linear Ub chains, endogenous NEMO interacts with Ubv-A in cell lysates (Figure 1F). The Ubv-A selectivity for binding to the UBAN domain of NEMO was also confirmed by phage ELISA using wild-type or mutant UBAN domains of NEMO, OPTN, ABIN1, and proteins involved in linear Ub chain generation and processing (Figure S1G). This selective binding of Ubv-A to UBAN of NEMO was further confirmed using surface plasmon resonance, revealing that Ubv-A binds to the UBAN of NEMO with ~7- and ~20-fold higher affinities than to the UBANs of OPTN and ABIN1, respectively (Figure S1H–S1J). Taken together, these experiments demonstrate that Ubv-A is a specific, high-affinity ligand for the NEMO UBAN domain.

## Ubv-A Binds the Functional Epitope on NEMO UBAN Domain

The phage display strategy was designed to generate variants that bind to the Ub-binding epitope on UBAN that naturally interacts with linear Ub chains. Indeed, a mutation of the phenylalanine 305 (F305) residue in murine UBAN that is required for interaction with linear Ub chains (matches to F312 of human UBAN) also abolished UBAN interaction with Ubv-A (Figure S2A and S2B). This indicates that Ubv-A may recognize an epitope on UBAN similar to the distal Ub within the linear Ub chain. To further confirm this, we crystallized human NEMO UBAN (hUBAN) in complex with Ubv-A and solved the crystal structure at 2.6 Å resolution by molecular replacement using UBAN domain (PDB: 3F89) as a search model. The apo form of hUBAN in our structure (PDB: 6YEK) shows the characteristic parallel coiled-coil homodimer with an overall length of approximately 115 Å (data not shown). The crystal structure of hUBAN in complex with Ubv-A (PDB: 6XX0) has two Ubv-A molecules per asymmetric unit (Figure 2A). Superimposition of the apo form and the Ubv-A bound form of hUBAN identified notable conformational changes, which caused an overall root-mean-square deviation (RMSD) of 3.1 Å between the two UBAN crystal structures (Figures 2B and S2C). The data collection and refinement statistics are summarized in Table 1.

It is well established that the distal Ub in linear 2xUb interacts with UBAN through its canonical hydrophobic isoleucine 44 (I44) patch (Rittinger and Ikeda, 2017). This interaction is also facilitated by the linear linkage between two Ub molecules, the non-canonical surface of proximal Ub, and the hydrophilic residues on UBAN (Figures 2C and S2D) (Rahighi et al., 2009). Interestingly, Ubv-A Region 2 residues significantly increase the hydrophobic patch area (accessible surface area [ASA] 774.81 Å$^2$) compared with the distal Ub of linear 2xUb (ASA 469.71 Å$^2$). This is driven, in large part, by a bulky hydrophobic F44 residue present in the center of the Ubv-A hydrophobic patch. Additionally, arginine 42 (R42) to I and K48 to methionine (M) mutations further increase the Ubv-A hydrophobic patch area (Figure 2C). This increased hydrophobicity likely accounts for the high affinity of Ubv-A for UBAN.

The protein design strategy of Region 3 resulted in the addition of amino acids at the Ubv-A C-terminal end (see Figure 1A). Unfortunately, our structure lacks the last five residues of the Ubv-A C terminus. Nevertheless, we observed that the hydroxyl group of serine 72 (S72) of Ubv-A and an α-carboxylic acid group of aspartate 311 (D311) of UBAN form a hydrogen bond. Additionally, Ubv-A leucine 73 (L73) is fully engaged by fitting in between two chains of the UBAN homodimer and interacts with tyrosine 308 (T308), K309, and F312 of UBAN. Our structure also indicates that R66 and Y68 of Ubv-A interact with glutamic acid 296 (E296) of UBAN through electrostatic interactions, which further stabilize complex formation (highlighted in Figure 2D). Importantly, back-to-wild-type Ubv-A single point mutations of residues 44, 66, 68, and 72 significantly decrease Ubv-A interaction with endogenous NEMO (Figures 2E and 2F). This supports the notion that the increased hydrophobicity and new electrostatic interactions formed between Ubv-A with UBAN underlie the high-affinity interaction.

## Ubv-A Attenuates NF-κB Signaling Activation

Superimposition of our hUBAN: Ubv-A structure (PDB: 6XX0) with the published mUBAN: 2xUb structure (PDB: 2ZVN) indicates that Ubv-A binds the UBAN epitope that is engaged by the distal Ub molecule within linear Ub chains (Figure 3A). This suggests that Ubv-A may act as a competitive inhibitor of linear Ub chain binding to NEMO, thereby attenuating NF-κB signaling activation in cells. To explore this, we first tested whether Ubv-A can inhibit the interaction between linear Ub chains and endogenous NEMO in total cell lysates. As expected, endogenous NEMO was efficiently pulled down from total cell lysates with glutathione S-transferase (GST)-4xUb linear chains but not with GST-1xUb or GST control (Figure 3B, lanes 1–3). Addition of purified 1xUb to cell lysates in excess had no effect on pull-down efficiency of NEMO by GST-4xUb (Figure 3B, lane 4). In sharp contrast, addition of varying concentrations of purified Ubv-A to cell extracts resulted in inhibition of NEMO pull-down by GST-4xUb in a concentration-dependent manner (Figure 3B, lanes 5–12). Similarly, Ubv-B was also able to inhibit NEMO pull-down by GST-4xUb in analogous competition experiments, albeit less effectively, in line with its reduced binding efficiency compared with Ubv-A (Figures S3A and S3B). In summary, these results illustrate that the generated high-affinity variants act as competitive inhibitors of linear Ub chain binding to NEMO in total cell extracts.

Given the observed competitive inhibition mediated by Ubv-A, we next examined the downstream biological effects. We evaluated the effects of Ubv-A on NF-κB signaling in cells by assessing the translocation of p65 transcription factor from the cytoplasm to the nucleus in TNFα-treated HeLa cells. As a control in these experiments, we used FLAG-tagged 1xUb that lacks the last two glycine (G) residues required to form Ub chains (UbΔGG). As expected, TNFα treatment led to p65 nuclear translocation in cells ectopically expressing the FLAG-UbΔGG control construct. In contrast, TNFα treatment of cells expressing the FLAG-Ubv-A construct was not able to induce p65 translocation to the nucleus (Figure 3C). Consistently, despite using the FLAG mean intensity per cell to select cells with similar Ub ΔGG or Ubv-A expression levels, the p65 nucleus-to-cytoplasm ratio was significantly lower in cells expressing Ubv-A relative to control cells (Figures 3D and 3E). This demonstrates that expression of Ubv-A in cells clearly attenuates NF-κB pathway activation. To further confirm this, we also measured the effect of Ubv-A expression on NF-κB transcriptional activity by using a luciferase

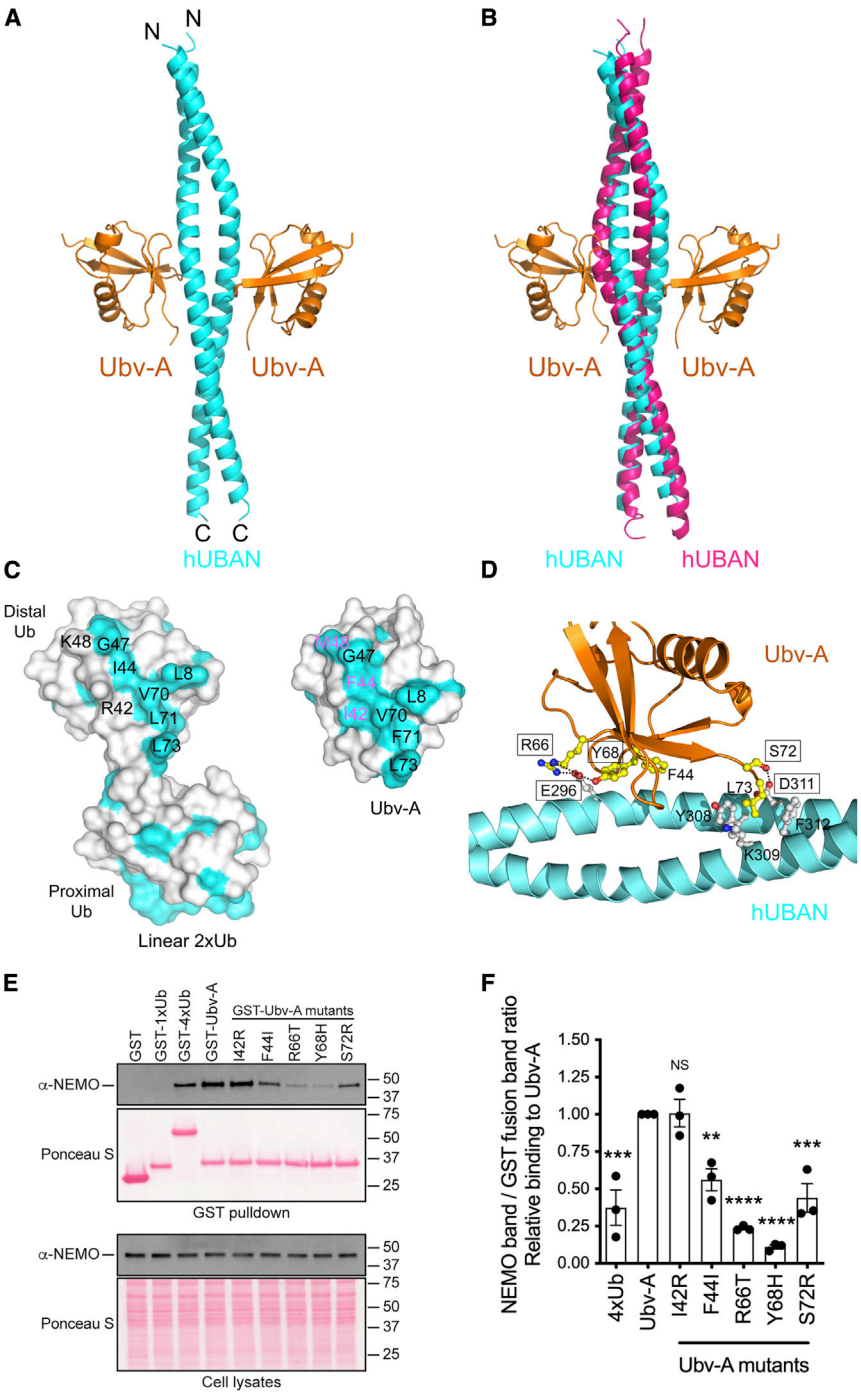


**Figure 2. Ubv-A Binds the Functional Epitope on NEMO UBAN Domain**

(A) The crystal structure of human NEMO UBAN domain in complex with Ubv-A at 2.6-Å resolution (PDB: 6XX0). Ribbon model of Ubv-A (orange) and human UBAN (hUBAN) (aquamarine). Two Ubv-A molecules bind C-terminal subdomain of hUBAN coiled-coil homodimer.

(B) Structural changes of hUBAN upon Ubv-A binding. Structural superimposition of the apo form of hUBAN (pink) and the hUBAN upon binding to Ubv-A (aquamarine and orange ribbon structures, respectively). See also Figure S2C.

(C) Surface representations of linear dimeric ubiquitin (2xUb) and Ubv-A. Hydrophobic residues are colored in aquamarine, wild-type residues are shown in black, whereas residues marked in pink denote Region 2 residues of the Ubv-A that affect the hydrophobic patch area. See also Figure S2D.

(D) Ubv-A binds hUBAN through its hydrophobic patch. Ribbon and ball-and-stick representation model of Ubv-A (orange) and hUBAN domain (aquamarine). Black lines linking between the atoms indicate hydrogen bonds and salt bridges. Residues highlighted in boxes indicate electrostatic interactions that stabilize complex formation. Other residues that contribute to this interaction are shown.

(E) A representative GST pull-down experiment using lysates of HEK293T cells and beads conjugated to either GST, GST-1xUb, GST-4xUb, GST-Ubv-A, or GST-Ubv-A back-to-wild-type mutants (n = 3). Ponceau staining and NEMO western blot are used as loading controls.

(F) Quantification of GST pull-down experiments presented in (E) (n = 3). The graph shows the ratio between the quantified intensity of the NEMO band relative to the corresponding GST fusion bands in GST pull-downs. Data normalized to the Ubv-A sample for comparison. One-way ANOVA multiple-comparison test was used for statistical analysis, while the level of significance was denoted as p values: 4xUb ***p = 0.0002, I42R not significant (NS; p = 0.99); F44I **p = 0.004; R66T ****p = < 0.0001; Y68H ****p = < 0.0001; S72R ***p = 0.0005. Data are presented as mean ± SEM.

reporter plasmid containing NF-κB response elements. In contrast to mock or Ub controls, expression of Ubv-A significantly reduced activation of the NF-κB luciferase reporter (Figure 3F). Furthermore, quantification of NF-κB target gene mRNA levels showed that expression of Ubv-A results in significant reduction of TNFα and NFKBIA/IκBα mRNA levels in comparison with Ub control (Figures 3G and 3H). Together, these data indicate that by disrupting the interaction between NEMO and linear Ub chains, Ubv-A attenuates activation of the NF-κB signaling pathway.

To assess whether Ubv-A affects other Ub-dependent pathways, we tested the effect of Ubv-A expression on epidermal growth factor receptor (EGFR) signaling in HCT116 cells. Our data reveal that, unlike the NF-κB pathway, Ubv-A does not affect the endocytosis or the degradation of EGFR (Figures S3C–S3E). This suggests that the effects of Ubv-A are specific to NF-κB signaling.

## Ubv-A as a Tool in Hit Discovery

Given the high-affinity binding of Ubv-A to UBAN, we envisioned that this enhanced interaction would enable cell-based assay development with a readout compatible with HTS. Importantly, since Ubv-A binds to the functionally relevant UBAN epitope, we hypothesized that a subset of chemical hits discovered using

**Table 1. Crystallization Data Collection and Refinement Statistics**

| | hNEMO-Ubv-A | hNEMO Apo |
|---|---|---|
| Data Collection Statistics | | |
| Beamline | SLS PX3 | EMBL-DESY P13 |
| Wavelength (Å) | 1.0000 | 0.97 |
| Space group | $P2_12_12$ | $P4_322$ |
| Unit cell (Å) | $a$ = 70.32, $b$ = 80.77, $c$ = 84.93<br>$\alpha$ = 90.00, $\beta$ = 90.00, $\gamma$ = 90.00 | $a$ = 85.76, $b$ = 85.76, $c$ = 99.01<br>$\alpha$ = 90.00, $\beta$ = 90.00, $\gamma$ = 90.00 |
| Resolution (Å) | 44.99–2.60 (2.74–2.60) | 85.76–3.20 (3.32–3.20) |
| Observed reflections | 101,221 (14,778) | 40,224 (4,126) |
| Unique reflections | 15,448 (2,213) | 6,469 (638) |
| Redundancy | 6.6 (6.7) | 6.2 (6.5) |
| Completeness (%) | 100.0 (100.0) | 99.7 (100.0) |
| $R_{merge}$ | 0.146 (1.212) | 0.032 (0.206) |
| $<I/\sigma I>$ | 10.7 (1.5) | 35.8 (8.2) |
| Refinement Statistics | | |
| Reflections in test set | 1,587 | 646 |
| $R_{cryst}$ | 23.8 | 29.1 |
| $R_{free}$ | 29.1 | 33.6 |
| No. of groups | | |
| Protein residues | 302 | 169 |
| Ions and ligand atoms | 0 | 0 |
| Water | 88 | 45 |
| Wilson $B$ factor | 53.7 | 103.9 |
| RMSD from ideal geometry | | |
| Bond length (Å) | 0.010 | 0.014 |
| Bond angles (°) | 1.309 | 1.86 |
| Ramachandran plot statistics | | |
| In favored regions (%) | 293 (99.66) | 152 (92.0) |
| In allowed regions (%) | 1 (0.34) | 10 (6.00) |
| Outliers (%) | 0 (0.00) | 3 (2.00) |
| PDB accession code | 6XX0 | 6YEK |

Values in parentheses are for the highest-resolution shell.

this approach might act through binding to UBAN, thereby leading to identification of compounds that might attenuate endogenous NF-κB signaling.

To identify such compounds, we developed a robust cell-based assay that is based on functional complementation of the small bit (SmBiT) and the large bit (LgBiT) of split nanoluciferase, the activity of which can be monitored in live cells (Figure 4A, NEMO assay). To reveal nanoluciferase modulators that represent false-positive hits, we also used a constitutively active nanoluciferase fusion (Figure 4A, control assay). Following the selection of the plasmid combination showing maximal assay activation (Figure S4A), we determined assay background by transfecting the LgBiT assay fusion together with a fusion of an unrelated protein (HaloTag) to SmBiT and the assay specificity by using the F312A mutant UBAN (Figure 4B). We also confirmed that the assay signal is indeed a readout for the high-affinity PPI between UBAN and Ubv-A, since back-to-wild-type mutations of Ubv-A residues that contribute to this interaction reduce assay activation (Figure 4C).

Next, we designed a screening cascade to facilitate the identification of high-confidence hits (Figure S4B). As a reference tool inhibitor in our HTS, we used Aloe Emodin that binds to UBAN, inhibits the PPI between UBAN and linear Ub chains, and shows activity in our NEMO cell-based assay (Figure S4C). This compound was identified previously using an *in vitro* approach with a library of naturally derived compounds (Vincendeau et al., 2016). We then screened a chemical library of 14,784 compounds comprising 66.7% PPI inhibitors and 33.3% diversity compounds at a single concentration against the NEMO assay with an average $Z'$ score of 0.42 (Figure S4D), demonstrating the advantages of using engineered high-affinity variants as tools in screening to create robust cell-based assays that are in line with current industry standards (Sui and Wu, 2007). Among the screened compounds, 352 active compounds were selected for confirmation and selectivity determination using NEMO and control assays, identifying 41 selective compounds (Figures S4E and S4F, and data not shown). Structural analysis of these compounds highlighted two chemical clusters and additional

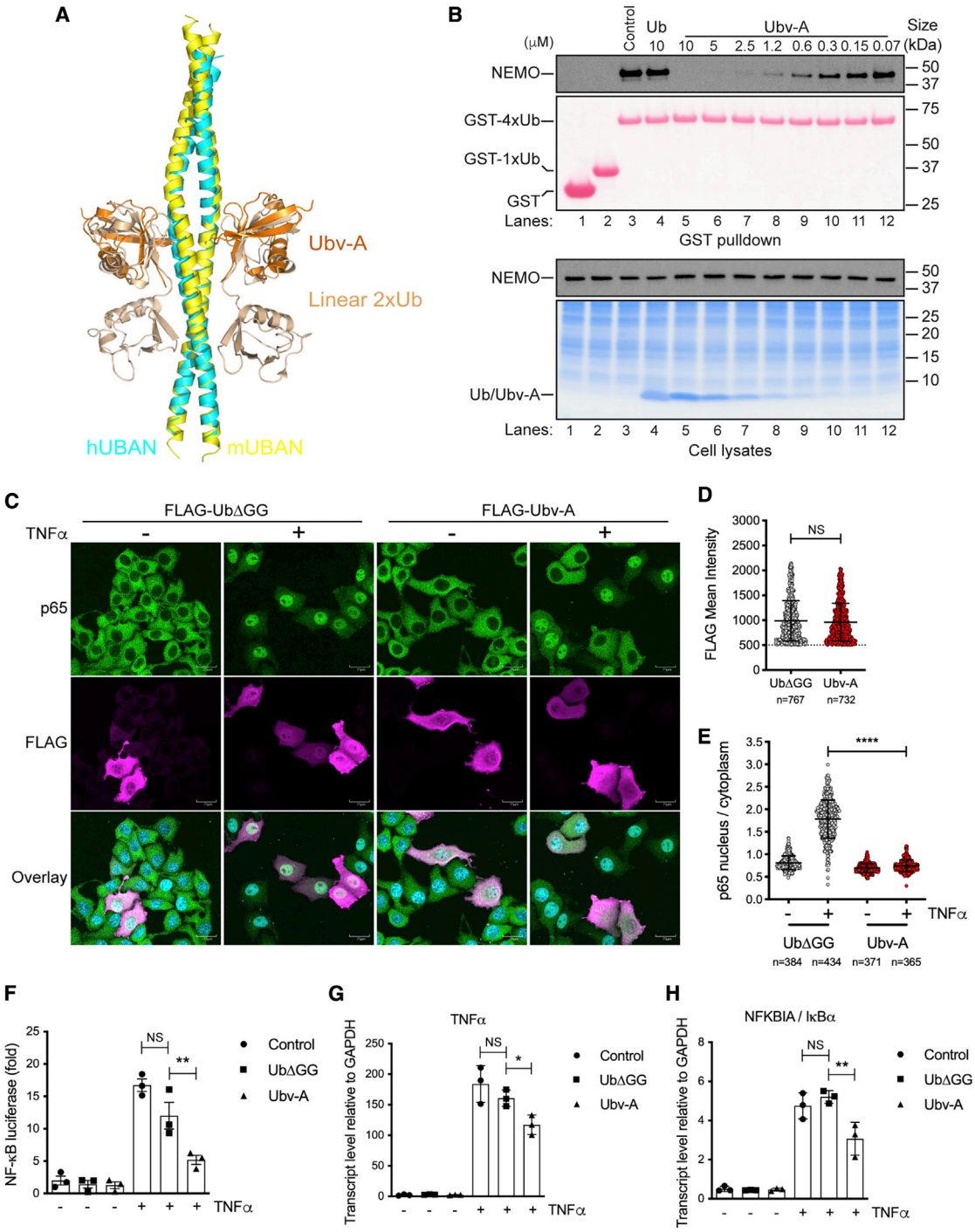


**Figure 3. Ubv-A Attenuates NF-κB Signaling Activation**

(A) Superimposition of murine UBAN (mUBAN in yellow) in complex with linear dimeric ubiquitin (2xUb in brown) (PDB: 2ZVN) and human UBAN (hUBAN in aquamarine) in complex with Ubv-A (orange) (PDB: 6XX0).

(B) GST competition assay between Ubv-A and linear 4xUb chains for binding to NEMO. Lysates of HEK293T cells were used for pull-downs using either GST, GST-1xUb, or GST-4xUb. Ubv-A was added to lysates of HEK293T cells at the indicated concentrations, and 10 μM Ub was used as control (n = 1). Ponceau staining, NEMO western blot, and Coomassie staining are used as loading controls.

(C) Representative confocal images of HeLa cells transiently transfected with either FLAG-tagged UbΔGG control or Ubv-A constructs. Following stimulation of cells with TNFα (25 ng/mL, 30 min), cells were fixed and used for immunostaining with anti-p65, anti-FLAG antibodies, and Hoechst. Scale bars, 25 μm.

(D) Quantification of FLAG mean intensity using data combined from three independent experiments. FLAG mean intensity threshold of 500 was applied to select FLAG-expressing cells in the combined dataset, and outliers were removed using the ROUT (Q = 1%) method. Unpaired t test was used for statistical significance; NS corresponds to non-significant p value of 0.1728. Data are presented as mean ± SD.

*(legend continued on next page)*

singletons that were selective against the NEMO assay (Figure 4D).

To reveal compounds that attenuate endogenous NF-κB signaling, we developed high-content imaging assay to assess the effect of top hits on p65 nuclear translocation in TNFα-treated HeLa cells using single-cell data analysis (average $Z'$ score 0.53 and data not shown). By screening our selective hit subset, we identified three compounds (T-10333, T-10334, and T-10336) that inhibited p65 translocation from the cytoplasm to the nucleus (Figures 4E and S4G) and were associated with low toxicity profiles when compared with the reference compounds TPCA-1 or cisplatin (Figures S4–S4I and Table S4). Using a high-sensitivity BLI assay, which allows the detection of small molecules binding to immobilized proteins, we confirmed that these hits show binding to UBAN. Out of these three compounds, T-10334 and T-10336 also displayed non-specific binding to the GST control, while T-10333 showed no binding to the GST control or Ubv-A, indicating high-specificity binding for UBAN (Figures S5A–S5C). Subsequently, we used saturation-transfer difference nuclear magnetic resonance (STD-NMR) to verify binding to UBAN. As shown in Figures 4F–4H, all three hits showed a clear STD signal, indicating a direct binding to the human NEMO UBAN domain. Altogether, this screening cascade demonstrates that Ubv-A enables robust HTS and facilitates identification of high-confidence chemical hits that can be used for further drug development.

## DISCUSSION

Robustness of HTS is a major determinant of success in drug discovery programs and ultimately in bringing future therapeutics to patients (Laraia et al., 2015). Drug targets, including natural PPIs that are a challenge, should be approached using several experimental methods maximizing chances for discovery of promising small molecule hits from diverse chemical libraries. In this study, we describe an approach for chemical screening whereby mutations are introduced directly into one binding partner of targeted PPI, generating a variant that binds to another protein partner of this PPI with increased affinity. When utilized in chemical screening, engineered variants can enable identification of small molecule inhibitors against natural PPIs.

We apply this approach to the interaction between linear Ub chains and NEMO, which is low-affinity PPI that regulates NF-κB pathway activation. Importantly, solved crystal structure validated that our protein engineering approach is hardwired to preserve binding of the variant to a functionally relevant epitope on the wild-type protein partner. The generated Ubv-A variant binds to the natural Ub-binding epitope on the UBAN domain of NEMO and acts as a competitive inhibitor of linear Ub chain binding, dampening NF-κB activation. Increased binding affinity of Ubv-A to UBAN enabled us to develop a robust cell-based HTS assay, which facilitated hit discovery from a relatively small chemical library, with the majority of compounds harboring PPI inhibitor properties. Triage assays revealed a subset of small molecule hits that directly bind to UBAN and attenuate endogenous NF-κB signaling in cells by inhibiting natural PPI.

Intracellular variants of naturally occurring binding partners developed by phage display have been widely used as effective tools for studying PPI functional epitopes, interrogation of signaling pathways, and monitoring of intracellular pathway activity (Ernst et al., 2013; Gorelik et al., 2016; Stolz et al., 2017; Wiechmann et al., 2017, 2020; Zhang et al., 2016). We anticipate that integrating protein engineering and chemical screening has the potential to expand the targetability of other therapeutically relevant but challenging targets. For example, this approach can be expanded to E3 Ub ligases with interesting platform technologies (Maculins et al., 2015) or to finding ligands for protein degraders (Lai and Crews, 2016).

An important consideration for future application of this approach is to provide a detailed characterization of the mechanism of action by which variants elicit their effects. At minimum, variants should be characterized structurally to validate their interaction with relevant epitopes on target proteins and biochemically to demonstrate selectivity binding. Additional characterization may include a demonstration of their effect upon overexpression on a given signaling pathway. We anticipate that this may represent a labor-intensive step in a hit discovery project. Nevertheless, we envisage that the approach reported in this study may initially be applied toward PPIs for which high-affinity variants have already been reported. Further application of this approach may include well-characterized signaling pathways that would be amenable to the development of rigorous triage assays and screening cascades. Ultimately, the future applications of this approach will be demonstrated by the discovery of lead compounds with significant biological activity in disease-relevant systems.

## SIGNIFICANCE

**High-throughput screening (HTS) technology platforms are broadly divided into biochemical and cell-based. Biochemical HTS is predominantly *in vitro* assays that offer the advantage of inhibiting protein-protein interactions (PPIs)**

(E) The graph shows the nucleus-to-cytoplasm ratio for p65 mean intensity in cells with FLAG mean intensity >500 in the combined dataset. Outliers were removed using the ROUT (Q = 1%) method. Ordinary one-way ANOVA multiple-comparison test was used for statistical analysis, for which the level of significance was denoted as ****$p < 0.0001$. Data are presented as mean ± SD.

(F) Renilla luciferase assay. HeLa cells were transiently transfected with mCherry, mCherry-tagged UbΔGG, or mCherry-Ubv-A together with NF-κB-luciferase and β-galactosidase reporters. After 36 h, cells were either left untreated or treated with TNFα (25 ng/mL, 5 h) before determining luciferase activity (n = 3). Ordinary one-way ANOVA multiple-comparison test was used for statistical analysis, for which the level of significance was denoted as **$p = 0.006$; NS corresponds to non-significant p value of 0.07. Data are presented as mean ± SEM.

(G and H) Ubv-A inhibits NF-κB target gene expression in HEK293T cells. Cells were transiently transfected with a control vector expressing mCherry or vectors expressing mCherry-tagged UbΔGG or Ubv-A. Cells were either left untreated or were treated with TNFα (25 ng/m, 5 h) 24 h post transfection and used for sample collection. Graphs show data from a representative experiment out of three different experiments. Ordinary one-way ANOVA multiple-comparison test was used for statistical analysis. The level of significance was denoted as follows. (G) NS corresponds to non-significant p value of 0.45; *$p = 0.03$. (H) NS corresponds to non-significant p value of 0.82; and **$p = 0.001$. Data are presented as mean ± SD.

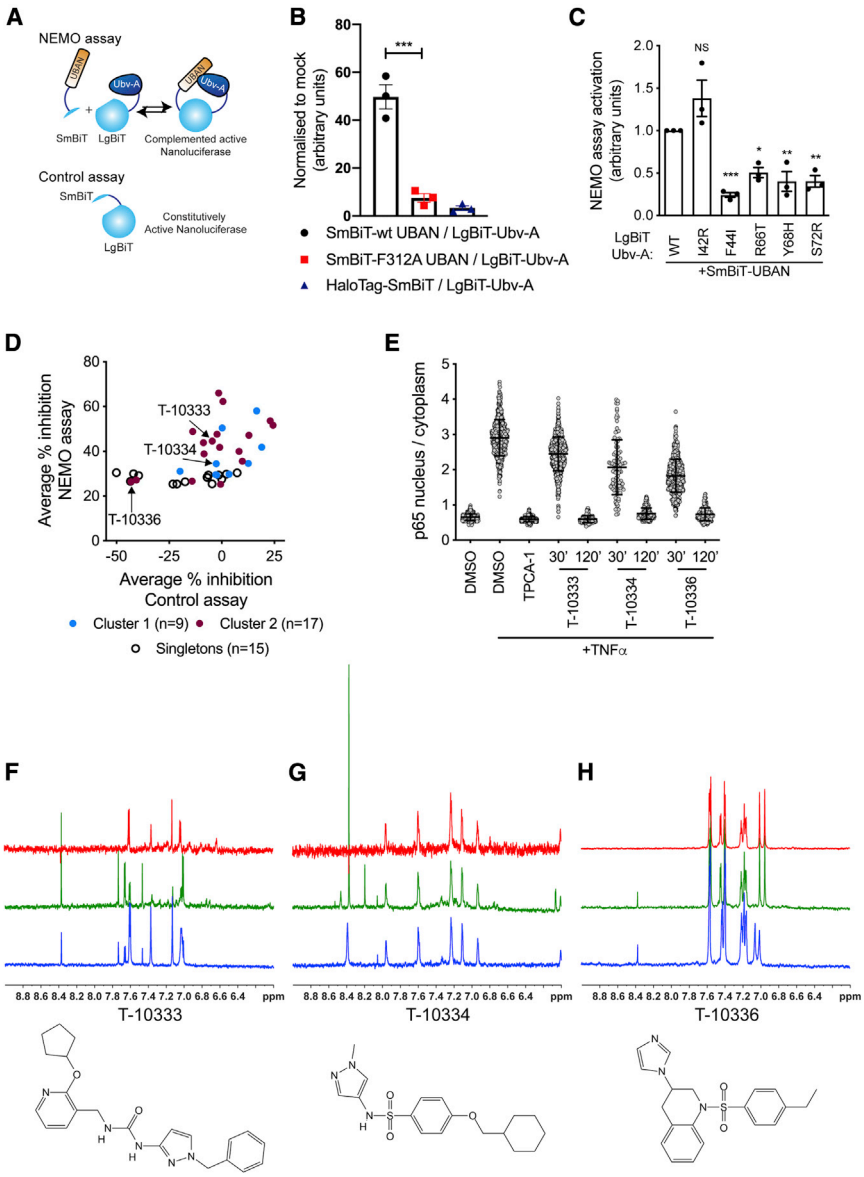


**Figure 4. Ubv-A As a Tool in Hit Discovery**

(A) A schematic representation of a cellular assay based on the NanoBiT system (Promega). The system vectors are modified to express human UBAN and Ubv-A as fusions to either small bit (SmBiT) or large bit (LgBiT) of split nanoluciferase. High-affinity PPI between UBAN and Ubv-A results in functional complementation of nanoluciferase, the activity of which can then be quantified in live cells.

(B) Assay validation. HEK293T cells were reverse transfected with assay constructs as indicated and nanoluciferase activity was assayed 20 h post transfection (n = 3). Ordinary one-way ANOVA multiple-comparison test was used for statistical analysis, for which the level of significance was denoted as ***p = 0.0002. Data are presented as mean ± SEM.

(C) NEMO assay activation is driven by high-affinity PPI. HEK293T cells reverse transfected with combinations of indicated assay vectors and NEMO assay activation are shown relative to UBAN/WT Ubv-A (n = 3). Ordinary one-way ANOVA with Tukey's multiple-comparisons test was used for statistical analysis. The levels of significance for assays using Ubv-A mutants are denoted as follows: Ubv-A I42R not significant (NS); Ubv-A F44I ***p = 0.0002; Ubv-A R66T *p = 0.0184; Ubv-A Y68H **p = 0.0032; Ubv-A S72R ** p = 0.0033. Data are presented as mean ± SEM.

(D) Selectivity assay results. Average percent (%) inhibition of NEMO and control assays is shown for a subset of n = 41 compounds (n = 3). Structural analysis identified Cluster 1 (blue circles, n = 9), Cluster 2 (purple circles, n = 17), and singletons (open circles, n = 15). Best hits are depicted on the graph.

(E) Quantification of high-content imaging assay results for top hits. HeLa cells were pre-incubated with T-10333, T-10334, and T-10336 (100 μM), TPCA-1 (10 μM), or DMSO control for either 30 min or 2 h prior treatment of cells with TNFα (25 ng/mL) for an additional 30 min. Cells were then fixed and processed for immunofluorescence imaging using anti-p65 antibody and Hoechst for nuclear staining. See Figure S4G for representative images (n = 1). Data are presented as mean ± SD.

(F–H) Saturation-transfer difference nuclear magnetic resonance (STD-NMR) experiments of hits were recorded in T-10333 (F), T-10334 (G), and T-10335 (H) in the presence of human UBAN. In each case a standard $^{1}$H excitation sculpting (ES) spectrum of the corresponding hit is shown as a blue spectrum (bottom). After addition of UBAN, another $^{1}$H ES spectrum was recorded and is presented as a green spectrum (middle). Finally, the STD experiment is presented in red (top). All compounds showed a significant STD signal, indicating interaction of these compounds with UBAN. Additionally, important chemical-shift perturbations or line broadening can be observed upon UBAN binding in most of the spectra. Corresponding compound chemical structures are depicted under the graphs, and compound CID numbers are shown in Method Details.

**or other targets in isolation. However, the availability of the individual components in sufficient quality and quantity is a limitation. Cell-based HTS circumvents this limitation via the expression of assay components *in situ*. In cells, targeted PPIs are in their native environment, providing additional advantages in chemical screening, such as understanding cell toxicity and permeability profiles for tested small molecules. However, the success of cell-based HTS is often hindered by weak binding affinity between protein partners, resulting in poor assay performance and a higher false-positive rate. This significantly complicates downstream triage experiments and identification of true hits, increasing the total costs associated with HTS campaigns. As such, it is common that naturally weak PPIs, even if representing therapeutically relevant targets, are essentially never considered for cell-based assay development because of the lack of robust HTS platforms. In this study we describe a method that facilitates identification of small molecule inhibitors against PPIs using cell-based HTS. Here we employ the phage display technology to generate a specific ubiquitin variant that binds to the molecular surface on NEMO with high affinity. This finding enabled us to develop a robust cell-based HTS assay, significantly reduce efforts in triaging hits, and identify true hits that bind to the relevant**

**epitope on NEMO. We believe that this approach will be widely utilized in chemical screening for hit identification against therapeutically relevant PPIs.**

## STAR★METHODS

Detailed methods are provided in the online version of this paper and include the following:

- KEY RESOURCES TABLE
- RESOURCE AVAILABILITY
  - Lead Contact
  - Materials Availability
  - Data and Code Availability
- EXPERIMENTAL MODEL AND SUBJECT DETAILS
  - Cell Lines
  - Bacterial Strains
- METHOD DETAILS
  - Cloning, Protein Expression and Purification
  - Phage Display Selections
  - GST Pulldowns
  - Western Blotting
  - EGF Receptor Stimulation Assay
  - NF-κB Luciferase Reporter Assay
  - Quantitative qRT-PCR
  - Immunofluorescence Microscopy
  - Mass Spectrometry
  - Protein Crystallization
  - X-ray Data Collection and Structure Determination
  - Surface Plasmon Resonance
  - Bio Layer Interferometry
  - STD-NMR
  - NanoBiT Assays
  - Compound Preparation
  - Compound Cluster Analysis
  - High Throughput Cellular NanoBiT Screen
  - Cell Viability Assay
- QUANTIFICATION AND STATISTICAL ANALYSIS

## SUPPLEMENTAL INFORMATION

Supplemental Information can be found online at https://doi.org/10.1016/j.chembiol.2020.07.010.

## ACKNOWLEDGMENTS

We thank Hadir Marei for comments on the manuscript and useful suggestions on experimental design. We thank Masuda Sader, Meike Hoffmeister, and Elena Veshkova for technical assistance, and Florian Bonn for assistance with IP-MS data analysis. We also acknowledge Katrin Rittinger and Daniel Durocher for reagents. We also thank Aditya Murthy and the department of Cancer Immunology at Genentech for support during final stages of manuscript preparation. This work was supported by the State of Hessen Landes-Offensive zur Entwicklung Wissenschaftlich-ökonomischer Exzellenz (LOEWE) Center for Translational Medicine and Pharmacology, TMP, and the Fraunhofer Cluster of Excellence for Immune Mediated Diseases (CIMD), and by grants from Else Kroener Fresenius Stiftung and Dr. Rolf M. Schwiete Stiftung (to I.D.).

## AUTHOR CONTRIBUTIONS

T.M. and I.D. designed the conceptual framework of the study and experiments. T.M. designed, performed, and analyzed experiments to characterize Ubv-A binding to UBAN and its mechanism of action, validate UBAN: Ubv-A crystal structure, HTS assays, the triage cascade, and hit validation. J.G.-P. studied the *in vitro* toxicity of hits, and contributed to structural characterization, STD-NMR experiments, analysis, and design of the experiments. A.S. contributed to the characterization of Ubv-A binding to UBAN and its mechanism of action. J.G. performed STD-NMR measurements. M.P. contributed to generation and characterization of UBAN binders. A.V. purified constructs for BLI assays. P.B. contributed to the purification of the NEMO UBAN domain used for structural studies and STD-NMR. G.V. contributed to Ubv-A IP-MS experiments. M.K. contributed to HTS assay development and performed HTS. A.Z. performed chemical analysis and selection of hits. S.R. demonstrated selectivity binding of Ubv-A to UBAN using SPR. V.S. investigated Ubv-A effect on EGFR signaling. M.J.P. contributed to HTS triage design. S.S.S. contributed to phage display design. A.E. contributed to phage display and conceptual study design. V.D. contributed to STD-NMR design. M.A. solved UBAN: Ubv-A crystal structure. T.M. wrote the manuscript with contributions from J.G.-P., A.E., M.A., and I.D., and comments from all authors.

## DECLARATION OF INTERESTS

T.M., A.E., M.P., M.K., and M.J.P. co-author a patent application for a part of this work (EP18191813.7 application number). T.M. is a current employee of Genentech. J.G,-P., A.V., M.K., A.Z., M.J.P., and I.D. are current employees of Fraunhofer Institutes. A.S. is a current employee of Pliva Croatia. M.P. is a current employee of Bio-Rad.

Received: May 21, 2020
Revised: June 24, 2020
Accepted: July 9, 2020
Published: July 28, 2020

## REFERENCES

Adams, P.D., Afonine, P.V., Bunkoczi, G., Chen, V.B., Davis, I.W., Echols, N., Headd, J.J., Hung, L.W., Kapral, G.J., Grosse-Kunstleve, R.W., et al. (2010). PHENIX: a comprehensive Python-based system for macromolecular structure solution. Acta Crystallogr. D Biol. Crystallogr. *66*, 213–221.

Arkin, M.R., Tang, Y., and Wells, J.A. (2014). Small-molecule inhibitors of protein-protein interactions: progressing toward the reality. Chem. Biol. *21*, 1102–1114.

Boncler, M., Różalski, M., Krajewska, U., Podsędek, A., and Watala, C. (2014). Comparison of PrestoBlue and MTT assays of cellular viability in the assessment of anti-proliferative effects of plant extracts on human endothelial cells. J. Pharmacol. Toxicol. Methods *69*, 9–16.

Cianci, M., Bourenkov, G., Pompidor, G., Karpics, I., Kallio, J., Bento, I., Roessle, M., Cipriani, F., Fiedler, S., and Schneider, T.R. (2017). P13, the EMBL macromolecular crystallography beamline at the low-emittance PETRA III ring for high- and low-energy phasing with variable beam focusing. J. Synchrotron Rad. *24*, 323–332.

Durant, J.L., Leland, B.A., Henry, D.R., and Nourse, J.G. (2002). Reoptimization of MDL keys for use in drug discovery. J. Chem. Inf. Comput. Sci. *42*, 1273–1280.

Emsley, P., Lohkamp, B., Scott, W.G., and Cowtan, K. (2010). Features and development of Coot. Acta Crystallogr. D Biol. Crystallogr. *66*, 486–501.

Ernst, A., Avvakumov, G., Tong, J., Fan, Y., Zhao, Y., Alberts, P., Persaud, A., Walker, J.R., Neculai, A.-M., Neculai, D., et al. (2013). A strategy for modulation of enzymes in the ubiquitin system. Science (New York, NY) *339*, 590–595.

García-Fernández, L., Garcia-Pardo, J., Tort, O., Prior, I., Brust, M., Casals, E., Lorenzo, J., and Puntes, V.F. (2017). Conserved effects and altered trafficking of Cetuximab antibodies conjugated to gold nanoparticles with precise control of their number and orientation. Nanoscale *9*, 6111–6121.

Gorelik, M., Orlicky, S., Sartori, M.A., Tang, X., Marcon, E., Kurinov, I., Greenblatt, J.F., Tyers, M., Moffat, J., Sicheri, F., and Sidhu, S.S. (2016).

Inhibition of SCF ubiquitin ligases by engineered ubiquitin variants that target the Cul1 binding site on the Skp1-F-box interface. Proc. Natl. Acad. Sci. U S A *113*, 3527–3532.

Gossert, A.D., and Jahnke, W. (2016). NMR in drug discovery: a practical guide to identification and validation of ligands interacting with biological macromolecules. Prog. Nucl. Magn. Reson. Spectrosc. *97*, 82–125.

Haas, T.L., Emmerich, C.H., Gerlach, B., Schmukle, A.C., Cordier, S.M., Rieser, E., Feltham, R., Vince, J., Warnken, U., Wenger, T., et al. (2009). Recruitment of the linear ubiquitin chain assembly complex stabilizes the TNF-R1 signaling complex and is required for TNF-mediated gene induction. Mol. Cell *36*, 831–844.

Humphrey, W., Dalke, A., and Schulten, K. (1996). VMD: visual molecular dynamics. J. Mol. Graph. *14*, 33–38.

Husnjak, K., and Dikic, I. (2012). Ubiquitin-binding proteins: decoders of ubiquitin-mediated cellular functions. Annu. Rev. Biochem. *81*, 291–322.

Iwai, K., and Tokunaga, F. (2009). Linear polyubiquitination: a new regulator of NF-kappaB activation. EMBO Rep. *10*, 706–713.

Johansson, H., Tsai, Y.-C.I., Fantom, K., Chung, C.-W., Kümper, S., Martino, L., Thomas, D.A., Eberl, H.C., Muelbaier, M., House, D., and Rittinger, K. (2019). Fragment-based covalent ligand screening enables rapid discovery of inhibitors for the RBR E3 ubiquitin ligase HOIP. J. Am. Chem. Soc. *141*, 2703–2712.

Kabsch, W. (2010). XDS. Acta Crystallogr. D Biol. Crystallogr. *66*, 125–132.

Katsuya, K., Oikawa, D., Iio, K., Obika, S., Hori, Y., Urashima, T., Ayukawa, K., and Tokunaga, F. (2019). Small-molecule inhibitors of linear ubiquitin chain assembly complex (LUBAC), HOIPINs, suppress NF-κB signaling. Biochem. Biophys. Res. Commun. *509*, 700–706.

Komander, D., and Rape, M. (2012). The ubiquitin code. Annu. Rev. Biochem. *81*, 203–229.

Lai, A.C., and Crews, C.M. (2016). Induced protein degradation: an emerging drug discovery paradigm. Nat. Rev. Drug Discov. *16*, 101–114.

Laraia, L., McKenzie, G., Spring, D.R., Venkitaraman, A.R., and Huggins, D.J. (2015). Overcoming chemical, biological, and computational challenges in the development of inhibitors targeting protein-protein interactions. Chem. Biol. *22*, 689–703.

Llona-Minguez, S., Baiget, J., and Mackay, S.P. (2013). Small-molecule inhibitors of IκB kinase (IKK) and IKK-related kinases. Pharm. Patent Anal. *2*, 481–498.

Lo, Y.-C., Lin, S.-C., Rospigliosi, C.C., Conze, D.B., Wu, C.-J., Ashwell, J.D., Eliezer, D., and Wu, H. (2009). Structural basis for recognition of diubiquitins by NEMO. Mol. Cell *33*, 602–615.

Maculins, T., Carter, N., Dorval, T., Hudson, K., Nissink, J.W.M., Hay, R.T., and Alwan, H. (2015). A generic platform for cellular screening against ubiquitin ligases. Sci. Rep. *6*, 18940.

Perkins, J.R., Diboun, I., Dessailly, B.H., Lees, J.G., and Orengo, C. (2010). Transient protein-protein interactions: structural, functional, and network properties. Structure *18*, 1233–1243.

Popovic, D., Vucic, D., and Dikic, I. (2014). Ubiquitination in disease pathogenesis and treatment. Nat. Med. *20*, 1242–1253.

Rahighi, S., Ikeda, F., Kawasaki, M., Akutsu, M., Suzuki, N., Kato, R., Kensche, T., Uejima, T., Bloor, S., Komander, D., et al. (2009). Specific recognition of linear ubiquitin chains by NEMO is important for NF-kB activation. Cell *136*, 1098–1109.

Rittinger, K., and Ikeda, F. (2017). Linear ubiquitin chains: enzymes, mechanisms and biology. Open Biol. *7*, 170026–170115.

Roberts, E., Eargle, J., Wright, D., and Luthey-Schulten, Z. (2006). MultiSeq: unifying sequence and structure data for evolutionary analysis. BMC Bioinformatics *7*, 382–411.

Ruiz, E.J., Diefenbacher, M.E., Nelson, J.K., Sancho, R., Pucci, F., Chakraborty, A., Moreno, P., Annibaldi, A., Liccardi, G., Encheva, V., et al. (2019). LUBAC determines chemotherapy resistance in squamous cell lung cancer. J. Exp. Med. *216*, 450–465.

Sakamoto, H., Egashira, S., Saito, N., Kirisako, T., Miller, S., Sasaki, Y., Matsumoto, T., Shimonishi, M., Komatsu, T., Terai, T., et al. (2015). Gliotoxin suppresses NF-κB activation by selectively inhibiting linear ubiquitin chain assembly complex (LUBAC). ACS Chem. Biol. *10*, 675–681.

Salim, N., Holliday, J., and Willett, P. (2003). Combination of fingerprint-based similarity coefficients using data fusion. J. Chem. Inf. Comput. Sci. *43*, 435–442.

Stolz, A., Putyrski, M., Kutle, I., Huber, J., Wang, C., Major, V., Sidhu, S.S., Youle, R.J., Rogov, V.V., Dötsch, V., et al. (2017). Fluorescence-based ATG8 sensors monitor localization and function of LC3/GABARAP proteins. EMBO J. *36*, 549–564.

Stumpf, M.P.H., Thorne, T., de Silva, E., Stewart, R., An, H.J., Lappe, M., and Wiuf, C. (2008). Estimating the size of the human interactome. Proc. Natl. Acad. Sci. U S A *105*, 6959–6964.

Sui, Y., and Wu, Z. (2007). Alternative statistical parameter for high-throughput screening assay quality assessment. J. Biomol. Screen. *12*, 229–234.

Taniguchi, K., and Karin, M. (2018). NF-κB, inflammation, immunity and cancer: coming of age. Nat. Publ. Group *18*, 309–324.

Tokunaga, F., Sakata, S.-I., Saeki, Y., Satomi, Y., Kirisako, T., Kamei, K., Nakagawa, T., Kato, M., Murata, S., Yamaoka, S., et al. (2009). Involvement of linear polyubiquitylation of NEMO in NF-kappaB activation. Nat. Cell Biol. *11*, 123–132.

Vincendeau, M., Hadian, K., Messias, A.C., Brenke, J.K., Halander, J., Griesbach, R., Greczmiel, U., Bertossi, A., Stehle, R., Nagel, D., et al. (2016). Inhibition of canonical NF-κB signaling by a small molecule targeting NEMO-ubiquitin interaction. Sci. Rep. *6*, 18934.

Wagner, S., Carpentier, I., Rogov, V., Kreike, M., Ikeda, F., Löhr, F., Wu, C.-J., Ashwell, J.D., Dötsch, V., Dikic, I., and Beyaert, R. (2008). Ubiquitin binding mediates the NF-κB inhibitory potential of ABIN proteins. Oncogene *27*, 3739–3745.

Wiechmann, S., Gärtner, A., Kniss, A., Stengl, A., Behrends, C., Rogov, V.V., Rodriguez, M.S., Dötsch, V., Müller, S., and Ernst, A. (2017). Site-specific inhibition of the small ubiquitin-like modifier (SUMO)-conjugating enzyme Ubc9 selectively impairs SUMO chain formation. J. Biol. Chem. *292*, 15340–15351.

Wiechmann, S., Maisonneuve, P., Grebbin, B.M., Hoffmeister, M., Kaulich, M., Clevers, H., Rajalingam, K., Kurinov, I., Farin, H.F., Sicheri, F., and Ernst, A. (2020). Conformation-specific inhibitors of activated Ras GTPases reveal limited Ras dependency of patient-derived cancer organoids. J. Biol. Chem. *295*, 4526–4540.

Winn, M.D., Ballard, C.C., Cowtan, K.D., Dodson, E.J., Emsley, P., Evans, P.R., Keegan, R.M., Krissinel, E.B., Leslie, A.G.W., McCoy, A., et al. (2011). Overview of the CCP4 suite and current developments. Acta Crystallogr. D Biol. Crystallogr. *67*, 235–242.

Yang, Y., Schmitz, R., Mitala, J., Whiting, A., Xiao, W., Ceribelli, M., Wright, G.W., Zhao, H., Xu, W., Rosenwald, A., et al. (2014). Essential role of the linear ubiquitin chain assembly complex in lymphoma revealed by rare germline polymorphisms. Cancer Discov. *4*, 480–493.

Yuki, K.E., Marei, H., Fiskin, E., Eva, M.M., Gopal, A.A., Schwartzentruber, J.A., Majewski, J., Cellier, M., Mandl, J.N., Vidal, S.M., et al. (2019). CYRI/FAM49B negatively regulates RAC1-driven cytoskeletal remodelling and protects against bacterial infection. Nat. Microbiol. *4*, 1516–1531.

Zhang, W., Wu, K.-P., Sartori, M.A., Kamadurai, H.B., Ordureau, A., Jiang, C., Mercredi, P.Y., Murchie, R., Hu, J., Persaud, A., et al. (2016). System-wide modulation of HECT E3 ligases with selective ubiquitin variant probes. Mol. Cell *62*, 121–136.

## STAR★METHODS

### KEY RESOURCES TABLE

| REAGENT or RESOURCE | SOURCE | IDENTIFIER |
|---|---|---|
| Antibodies | | |
| anti-α-Tubulin antibody | Sigma-Aldrich | Sigma-Aldrich Cat# T9026; RRID:AB_477593 |
| Anti-HA High Affinity; Rat monoclonal antibody (clone 3F10) | Roche | Roche Cat# 11867431001; RRID:AB_390919 |
| IKK (DA10-12) Mouse mAb antibody | Cell Signaling Technology | Cell Signaling Technology Cat# 2695; RRID:AB_2124826 |
| GAL4 (DBD) (RK5C1) antibody | Santa Cruz Biotechnology | Santa Cruz Biotechnology Cat# sc-510; RRID:AB_627655 |
| EGFR (528) antibody | Santa Cruz Biotechnology | Santa Cruz Biotechnology Cat# sc-120; RRID:AB_627492 |
| Mouse Anti-Chicken Vinculin Monoclonal Antibody, Unconjugated, Clone VIN-11-5 | Sigma-Aldrich | Sigma-Aldrich Cat# V4505; RRID:AB_477617 |
| anti-tRFP antibody | Evrogen | Evrogen Cat# AB233; RRID:AB_2571743 |
| Anti-rat IgG, HRP-linked Antibody | Cell Signaling Technology | Cell Signaling Technology Cat# 7077; RRID:AB_1069471 |
| Goat Anti-Mouse Goat anti-mouse IgG-HRP Polyclonal, Hrp Conjugated antibody | Santa Cruz Biotechnology | Santa Cruz Biotechnology Cat# sc-2005; RRID:AB_631736 |
| Goat Anti-Rabbit Immunoglobulins/HRP antibody | Agilent | Agilent Cat# P0448; RRID:AB_2617138 |
| Monoclonal ANTI-FLAG® M2 antibody | Sigma-Aldrich | Sigma-Aldrich Cat# F3165; RRID:AB_259529 |
| NFkappaB p65 (F-6) antibody | Santa Cruz Biotechnology | Santa Cruz Biotechnology Cat# sc-8008; RRID:AB_628017 |
| Donkey Anti-Mouse IgG (H+L) Antibody, Alexa Fluor 488 Conjugated | Molecular Probes | Molecular Probes Cat# A-21202; RRID:AB_141607 |
| Donkey anti-Mouse IgG (H+L) Highly Cross-Adsorbed Secondary Antibody, Alexa Fluor 647 | Thermo Fisher Scientific | Thermo Fisher Scientific Cat# A-31571; RRID:AB_162542 |
| Goat anti-Mouse IgG (H+L) Cross-Adsorbed Secondary Antibody, Alexa Fluor 488 | Thermo Fisher Scientific | Thermo Fisher Scientific Cat# A-11001; RRID:AB_2534069 |
| Bacterial and Virus Strains | | |
| *Escherichia coli*: T7 Express | New England Biolabs | Cat#C2566I |
| *Escherichia coli*: Rosetta BL21 DE3 | Millipore Sigma | Cat#70954 |
| Chemicals, Peptides, and Recombinant Proteins | | |
| Dulbecco's Modified Eagle Medium | ThermoFisher Scientific | Cat#11960-044 |
| Penicillin-streptomycin | Millipore Sigma | Cat#P0781-100ml |
| Fetal bovine serum | ThermoFisher Scientific | Cat#10270106 |
| Glutathione Sepharose 4B affinity resin | GE Healthcare | Cat#17-0756-01 |
| C3 PreScission protease | GE Healthcare | Cat#27084301 |
| HiLoad 16/600 Superdex 200 | GE Healthcare | Cat#28989335 |
| HiLoad 16/600 Superdex 75 | GE Healthcare | Cat#28989334 |
| TALON Metal Affinity resin | Takara Clontech | Cat#635504 |
| 2x Laemmli sample buffer | Bio-Rad | Cat#1610737 |
| 4–20% Mini-PROTEAN® TGX Stain-Free™ Protein Gels | Bio-Rad | Cat#4568096 |
| X-ray films | VWR | Cat#28-9068-44 |
| Genejuice Transfection Reagent | Millipore Sigma | Cat#70967 |
| EGF | Peprotech | Cat#AF-100-15 |
| 4% paraformaldehyde solution in PBS | Santa Cruz Biotechnology | Cat#SC281692 |
| Recombinant human TNFalpha | Peprotech | Cat#300-01A |

(*Continued on next page*)

*Continued*

| REAGENT or RESOURCE | SOURCE | IDENTIFIER |
|---|---|---|
| LC-480 SybrGreen PCR mix | Roche Diagnostics | Cat#04707516001 |
| 96-well flat bottom tissue culture-treated microplates | Greiner Bio | Cat#655090 |
| Hoechst 33342 | Life Technologies | Cat#R37605 |
| HA-agarose beads | Sigma Millipore | Cat#A2095 |
| HA peptide | Sigma Millipore | Cat#I2149 |
| mono ubiquitin | Millipore Sigma | Cat#U6253 |
| di-ubiquitin K48-linked chains | Boston Biochem | Cat#UC-200B |
| di-ubiquitin K63-linked chains | Boston Biochem | Cat#UC-300B |
| linear di-ubiquitin chains | Boston Biochem | Cat#UC-700B |
| Aloe Emodin | Millipore Sigma | Cat#93938 |
| TPCA-1 | Millipore Sigma | Cat#T1452 |
| White 384-well tissue culture–treated microplates | Greiner Bio-One | Cat#781073 |
| PrestoBlue™ Cell Viability Reagent | ThermoFisher Scientific | Cat#A13261 |
| Critical Commercial Assays | | |
| PathDetect NF-kB Cis-Reporting System | Agilent Technologies | Cat#219077 |
| QuikChange II XL Site-Directed Mutagenesis Kit | Stratagene | Cat#200517 |
| Qiagen RNAEasy kit | Qiagen | Cat#74104 |
| RevertAid First Strand cDNA Synthesis Kit | ThermoFisher Scientific | Cat#K1621 |
| NanoBiT® PPI MCS Starter System | Promega | Cat#N2014 |
| Nano-Glo® Live Cell Assay System | Promega | Cat#N2012 |
| Deposited Data | | |
| Crystal structure of NEMO in complex with Ubv-A | This paper | PDB: 6XX0 |
| Crystal structure of human NEMO apo form | This paper | PDB: 6YEK |
| Crystal structure of mouse NEMO UBAN | (Rahighi et al., 2009) | PDB: 3F89 |
| Crystal structure of mouse NEMO UBAN with linear dimeric ubiquitin | (Rahighi et al., 2009) | PDB: 2ZVN |
| Raw Western Blot data | Mendeley Data | https://doi.org/10.17632/34w3cxwd9v.1 |
| Experimental Models: Cell Lines | | |
| HeLa | ATCC | ATCC Cat# CCL-2; RRID:CVCL_0030 |
| HEK293T | ATCC | ATCC Cat# CRL-3216; RRID:CVCL_0063 |
| U2OS | ATCC | ATCC Cat# HTB-96; RRID:CVCL_0042 |
| U2OS, TetR, 1xUbG76V-HA | This study | N/A |
| U2OS, TetR, Ubv-A-HA | This study | N/A |
| A-549 | ATCC | ATCC Cat# CCL-185; RRID:CVCL_0023 |
| Oligonucleotides | | |
| See Table S2 for PCR primers used in this study. | N/A | N/A |
| Recombinant DNA | | |
| See Table S1 and S3 for details. | N/A | N/A |
| Software and Algorithms | | |
| GraphPad Prism 8.0 | GraphPad Software, USA | https://www.graphpad.com |
| Coot | (Emsley et al., 2010) | https://www2.mrc-lmb.cam.ac.uk/personal/pemsley/coot/ |
| Phenix | (Adams et al., 2010) | http://www.phenix-online.org/ |
| CCP4 | (Winn et al., 2011) | http://www.ccp4.ac.uk |
| MACCS Keys | (Durant et al., 2002) | http://www.mayachemtools.org/index.html |
| KNIME v.3.7.1 | (Salim et al., 2003) | https://www.knime.com |
| RDKit | Open-Source Cheminformatics Software | http://www.rdkit.org |
| Bruker TopSpin 4.0 Software | Bruker | https://www.bruker.com/ |

(*Continued on next page*)

*Continued*

| REAGENT or RESOURCE | SOURCE | IDENTIFIER |
|---|---|---|
| Visual Molecular Dinamics (VMD) v. 1.9.3 | (Humphrey et al., 1996) | https://www.ks.uiuc.edu/ |
| MuliSeq 2.0 1.9.3 | (Roberts et al., 2006) | https://www.ks.uiuc.edu/Research/vmd/plugins/multiseq/ |
| PyMOL v. 2.0 | Schrödinger, LLC. | https://pymol.org/2/ |

## RESOURCE AVAILABILITY

### Lead Contact

Further information and requests for resources and reagents should be addressed to and will be fulfilled by the Lead Contact, Ivan Dikic (dikic@biochem2.uni-frankfurt.de).

### Materials Availability

Newly generated plasmids and cell lines in this study will be made available upon request.

### Data and Code Availability

The accession numbers for the protein structures reported in this paper have been deposited in Protein Data Bank (http://www.rcsb.org/pdb): 6YEK and 6XX0. Original data have been deposited to Mendeley Data: [https://doi.org/10.17632/34w3cxwd9v.1].

## EXPERIMENTAL MODEL AND SUBJECT DETAILS

### Cell Lines

Human HeLa (ATCC CCL-2, female), HEK293T (ATCC CRL-3216, female), U2OS (ATCC HTB-96, female) and A-549 (ATCC CCL-185, male) cell lines were obtained from the American Type Culture Collection (ATCC). All cell lines were maintained at 37°C and 5% $CO_2$ and cultured in Dulbecco's Modified Eagle Medium (DMEM, ThermoFisher Scientific, 11960-044) supplemented with 10 μg/ml penicillin-streptomycin (Millipore Sigma, P0781-100ml) and 10% v/v fetal bovine serum (FBS, ThermoFisher Scientific, 10270106) or without FBS for experiments using serum starvation. U2OS cell lines with dox-inducible expression were generated using Retro-X™ Tet-On Advanced Inducible Expression System (Clontech, 632104) using manufacturer's instructions.

### Bacterial Strains

*Escherichia coli* (*E.coli*) DH5α strains were used for plasmid amplification. *E.coli* DH5α cells were grown in LB medium at 37°C. *E.coli* T7 Express (New England Biolabs, C2566I) or *E.coli* Rosetta BL21 DE3 (Millipore Sigma, 70954) strains were used for protein purification for biochemistry or crystallography. Cells were grown at 37°C until $OD_{600}$ of 0.5, followed by induction with 0.25 or 0.5 mM isopropyl-β-d-thiogalactoside (IPTG) at 18°C for 16-20 hours.

## METHOD DETAILS

### Cloning, Protein Expression and Purification

Cloning details of DNA fragments and usage of constructs in this study are described in Table S1. PCR primers used for cloning of constructs are described in Table S2. The sequence of synthetic gene fragments is presented in Table S3. GST or His-tagged fusion protein expression was done using *E.coli* T7 Express (New England Biolabs, C2566I) or *E.coli* Rosetta BL21 DE3 (Millipore Sigma, 70954). For purification of $^{15}$N-labelled human NEMO UBAN domain the construct was expressed in M9 minimal medium with a controlled $^{15}$N carbon source. Following IPTG induction, cells were lysed by sonication in lysis buffer (25 mM Tris, 200 mM NaCl, 0.5% Triton X-100, 1 mg/ml lysozyme, EDTA-free protease inhibitor cocktail (Roche Diagnostics, Mannheim, Germany), 1 mM PMSF, 5 mM DDT (for GST tagged proteins) or 5 mM TCEP (for His-tagged proteins), pH 8.5), incubated for 1 hour rotating on 4°C and then lysates were cleared by centrifugation. For protein crystallization, the expressed proteins were purified by Glutathione Sepharose 4B affinity resin (GE Healthcare, 17-0756-01), washed, cleaved by C3 PreScission protease (GE Healthcare, 27084301), and purified by size exclusion chromatography using HiLoad 16/600 Superdex 200 (GE Healthcare, 28989335) for NEMO UBAN or HiLoad 16/600 Superdex 75 column (GE Healthcare, 28989334) for Ubv-A and Ubv-B in 25 mM Tris, 200 mM NaCl, pH 8.0. For BLI assays to assess binding of ubiquitin variants to UBAN and biochemical competition assays, Ubv-A and Ubv-B were purified as HIS-tagged fusions using TALON Metal Affinity resin (Takara Clontech, 635504). For BLI assays to assess binding of small molecules, Glutathione Sepharose 4B affinity resin with immobilized GST fusions was thoroughly washed and GST-fusions were eluted using elution buffer (200 mM imidazole, 25 mM Tris, 200 mM NaCl, 5 mM TCEP; pH 7.5). For GST pulldown assays, GST-fusions were left on the beads after washes. Mutations were introduced with the QuikChange II XL Site-Directed Mutagenesis Kit (Stratagene, 200517) and confirmed by DNA sequencing. Mutants were overexpressed and purified as the wild type constructs as above.

### Phage Display Selections

The phage displayed ubiquitin variant library used in this study was generated using soft randomization strategy as published previously (Ernst et al., 2013). Phage display selections were performed using published methods (Ernst et al., 2013). In brief, the murine NEMO UBAN domain was expressed as GST fusion protein, purified from *E.coli* BL21 (DE3) strain and immobilized by direct adsorption on an ELISA plate. For selection of high affinity ubiquitin variants, the phage library was pre-adsorbed on immobilized GST or BSA (2 μM) at 4°C to remove unspecific binding variants and the supernatant was transferred to immobilized NEMO UBAN domain at 22°C. After washing 10 times with PBS, bound phage was eluted by addition of 0.1 M HCl (pH 2.2), immediately neutralized using 1 M Tris and used to infect XL1 Blue. Phage was prepared as before (Ernst et al., 2013) and used for a next round of enrichment on immobilized NEMO. To increase stringency in subsequent selection rounds, the concentration of antigen was gradually decreased from the initial 2 μM in the first round to 0.25 μM in the 5$^{th}$ and last round. Furthermore, the number of washes was increased by two additional washes in each round to 18 times in the last round. After selection, the pool of ubiquitin variants was screened for binding using established protocols (Ernst et al., 2013), yielding 23 unique variants with improved affinity to NEMO relative to ubiquitin wild type. To further triage this ensemble of NEMO binding ubiquitin variants, the half-maximal concentration ($IC_{50}$) of binding was estimated using a competition ELISA protocol. In brief, the clonal populations of individual phage displaying a NEMO binding ubiquitin variant were incubated with decreasing concentration of NEMO or sample buffer (PBS) for 2 hours in a non-protein binding microtiter plate and then transferred to a microtiter plate coated with NEMO at 2 μM. After incubation for 15 min at 22°C, bound phage was detected as described before (Ernst et al., 2013). The two best binding variants Ubv-A and Ubv-B were characterized further.

### GST Pulldowns

GST pulldowns were performed essentially as described previously (Yuki et al., 2019). Briefly, *E.coli* Rosetta BL21 DE3 competent cells (Millipore Sigma, 70954) were used to grow and purify the respective GST-tagged proteins as described above. GST fusions immobilized on Glutathione Sepharose 4B (GE Healthcare, 17-0756-01) were washed using GST lysis buffer (25 mM Tris-HCL pH 7.2, 150 mM NaCl, 5mM $MgCl_2$, 1% Nonidet P40 (v/v), 5% glycerol (v/v), 1% protease inhibitor cocktail tablet (Roche, 4693132001), 1% phosphatase inhibitor cocktails 1 and 2 (v/v; Millipore Sigma, P5726-5ml and P0044-5ml) in $dH_2O$). Cells were lysed 24 hours post transfection in GST lysis buffer and equal protein amounts were incubated with empty or conjugated GST Sepharose resin as indicated for 2 hours at 4°C. Beads were washed following incubation at least five times for 5-10 minutes and prepared for western blotting.

### Western Blotting

Samples were mixed with the appropriate volume of 2x Laemmli sample buffer (Bio-Rad, 1610737) and resolved on 4–20% Mini-PROTEAN® TGX Stain-Free™ Protein Gels (Bio-Rad, 4568096). Pre-stained protein ladder (BioFroxx, 1123YL500) was run alongside the samples for protein size reference. Proteins were transferred onto PVDF membranes (Millipore, IPFL00010). Western blotting was performed using antibodies listed in Key Resource Table and visualized using X-ray films (VWR, 28-9068-44) and the western blotting luminol reagent (Santacruz Biotechnology, sc-2048 and sc-2049).

### EGF Receptor Stimulation Assay

HCT116 cells were transfected with the indicated constructs using Genejuice Transfection Reagent (Millipore Sigma, 70967) according to the manufacturer instructions. After 24 hours cells were serum-starved overnight and treated with EGF 100 nM (Peprotech, AF-100-15) for the indicated times. For immunofluorescence assays cells were fixed with 4% paraformaldehyde solution in PBS (Santacruz, SC281692) for 15 min and stained using anti-EGFR primary antibody (Santacruz Biotechnology, sc-120), which was detected using Alexa 647-conjugated donkey anti-mouse secondary antibody (ThermoFisher Scientific A-31571). For time course analysis, HCT116 cells lysates were prepared using cell lysis buffer (50 mM Tris, 1 mM EDTA, 1% SDS, 25 mM NaF, pH 7.2) complemented with protease inhibitor cocktail (Roche, 4693132001) and phosphatase inhibitor cocktail 3 (Millipore Sigma, P0044) and processed for western blot analysis.

### NF-κB Luciferase Reporter Assay

HeLa cells were transiently co-transfected with plasmids containing luciferase pNFκB-luc (Agilent Technologies, 219077), β-galactosidase pUT651 and mCherry empty vector, mCherry-Ub wild type or mCherry-Ubv-A. 24 hours after transfection, cells were starved in DMEM. 36 hours after transfection, cells were either left untreated or treated with TNF-α at 20 ng/ml for 5 hours (Peprotech, 300-01A). Upon treatment, cells were lysed and subjected to luciferase assay following manufacturer's protocol. β-galactosidase activity on its substrate was used as internal control.

### Quantitative qRT-PCR

Whole cell RNA samples were isolated using Qiagen RNAEasy kit (Qiagen, 74104). 2 μg RNA was transcribed with RevertAid First Strand cDNA Synthesis Kit (ThermoFisher Scientific, K1621) according to the manufacturer's protocol, using Oligo $(dT)_{18}$ primers. cDNA generated from DNA-free RNA samples by reverse transcription was analyzed using LC-480 SybrGreen PCR mix (Roche Diagnostics, 04707516001) on a LC480 II Lightcycler system (Roche Diagnostics, 05015278001). Primers used in the experiment were: NFKBIA/IκBα_Fw 5'- CCGCACCTCCACTCCATCC-3', NFKBIA/IκBα_Rev 5'-ACATCAGCACCCAAGGACACC-3', TNFα_Fw 5'-CCCAGGGACCTCTCTCTAATCA-3', TNFα_Rev 5'-GCTACAGGCTTGTCACTCGG-3'. Quantification of NF-κB target genes was

done with GAPDH as a control. Detected cDNA signal from unstimulated mCherry transfected cells was used as a relative reference for other detected signals. Experiments were repeated three individual times. Each qPCR reaction was run in duplicate or triplicate.

### Immunofluorescence Microscopy

HeLa cells were plated in 96-well flat bottom tissue culture-treated microplates (Greiner Bio, 655090), transfected as indicated using Genejuice Transfection Reagent (Millipore Sigma, 70967), 24 hours post-transfection media was exchanged to serum starvation media overnight. For compound treatment, cells were treated with DMSO or compounds as indicated followed by cell treatment with 25 ng/ml of recombinant TNF-$\alpha$ (Peprotech, 300-01A) for 30 min, then fixed with 4% paraformaldehyde solution in PBS (Santacruz, SC281692) for 15 min at room temperature. Cells were then permeabilized with 0.25% Triton-X (v/v) in PBS for 5 min at room temperature. For fluorescence staining, cells were next blocked in 10% FBS for 40 min prior to incubation with either Alexa Fluor® 488 conjugated anti-p65 (Santacruz Biotechnology, sc-8008 AF488) or unconjugated anti-FLAG (Millipore Sigma, F3165) primary antibodies (in 1% FBS, 0.05% Triton-X (v/v)) for 1 hour at room temperature. In the case of anti-FLAG staining, the Alexa Fluor® 488 secondary antibody (ThermoFisher Scientific, A-11001) was then added for an additional 1 hour at room temperature in the dark before staining with Hoechst 33342 (Life Technologies, R37605). Images were captured using the Yokogawa CQ1 confocal quantitative image cytometer platform (x 40 magnification) and images were analyzed using the built-in CQ1 image analysis software. For cells expressing FLAG-tagged UbΔGG or Ubv-A constructs, the FLAG staining was used to determine the expression levels. For analysis of cells based on FLAG expression levels, the FLAG staining in untransfected cells was used to generate the intensity threshold that determined the background staining. Individual cells with FLAG intensity above this threshold were selected from transfected samples and combined cell populations from three independent experiments were further analyzed for the p65 translocation ratio.

### Mass Spectrometry

U2OS cells with inducible expression of either HA-tagged UbΔGG or Ubv-A were plated into 2 x 150 $cm^2$ dishes with 7.5 x $10^6$ cells / dish in media containing 1 $\mu$g/ml doxycycline. Cells were scraped into PBS 24 hours post-plating, pooled, and washed twice in PBS and pelleted by centrifugation. After centrifugation, the cell pellets were resuspended in lysis buffer (50 mM Tris / HCl, pH 7.5, 150 mM NaCl, 0.5% Nonidet P-40 containing protease inhibitor cocktail (Roche, 4693132001)) and incubated for 30 min at 4°C with rotation. The lysates were centrifuged, and supernatants were transferred to pre-equilibrated HA-agarose beads (Sigma Millipore, A2095) and incubated overnight at 4°C. Beads were washed 5 times with 1 ml of lysis buffer and 5 times with PBS. Elution was performed by incubating the beads with 50 $\mu$l of HA peptide diluted at 250 $\mu$g/ml (Sigma Millipore, I2149). Eluates were combined, and further steps of sample preparation for trypsin digest and mass spectrometry were done as described previously (Wiechmann et al., 2017).

### Protein Crystallization

The crystals of human NEMO UBAN domain (hUBAN) in complex with Ubv-A were grown using sitting drop vapor diffusion with a reservoir solution containing 22.5% polyethylene glycol 3350, 0.1 M magnesium chloride, 0.1 M Tris-HCl, pH 7.0 at 293K. The crystals of hUBAN apo form were obtained using hanging drop vapor diffusion by mixing equivalent volumes of the protein sample concentrated to 23 mg/ml with a reservoir solution containing 45% ethylene glycol and 50 mM acetate, pH 4.0. hUBAN crystals appeared after 1 day incubation at 293K. hUBAN-Ubv-A crystals were flash-cooled using 25% polyethylene glycol 400 in the reservoir solution as cryoprotectant.

### X-ray Data Collection and Structure Determination

In the case of hUBAN-Ubv-A complex diffraction data were collected at Swiss Lightsource SLS, beam line PXIII and processed with XDS (Kabsch, 2010). Diffraction data for hUBAN were collected at beamline p13 operated by EMBL Hamburg at the PETRA III storage ring (DESY, Hamburg, Germany) (Cianci et al., 2017). The crystal structures were determined by molecular replacement using the murine NEMO UBAN structure (PDB: 3F89) as a search model. Manual model building and refinement were done with Coot, CCP4 software suite and Phenix (Adams et al., 2010; Emsley et al., 2010; Winn et al., 2011). The final statistics of refined models are shown in Table 1 and the corresponding atomic coordinates have been deposited in the Protein Data Bank (Accession No. 6XX0 and No 6YEK). The RMSD analysis in the structure-based alignment of hUBAN bound to Ubv-A and hUBAN on its apo form was performed using VMD (Humphrey et al., 1996) and MultiSeq 2.0 (Roberts et al., 2006).

### Surface Plasmon Resonance

SPR experiments were performed using the BiOptix 404pi instrument (BiOptix). GST-tagged fusions were immobilized on a Xantech CMD200m sensor chip. Various concentrations of His-tagged Ubv-A were prepared in a running buffer containing 10 mM HEPES, pH 7.4 supplemented with 3 mM EDTA, 150 mM NaCl and 0.005% Tween 20. Each experiment was repeated three times and data was analyzed using Scrubber 2 (BioLogic Software).

### Bio Layer Interferometry

An Octet Red instrument (Fortebio, Inc., Menlo Park, CA) was used for all assay development and subsequent binding studies. Data were analyzed using the Fortebio Octet RED analysis software or exported for analysis and presentation in other software packages. All kinetic assays were done with samples diluted in freshly prepared assay buffer containing 1 mg/mL BSA in PBS supplemented

with 0.05% Tween-20. Kinetic assays were performed by first capturing human UBAN fused to GST on anti-GST biosensors followed by at least two baseline steps of 30 seconds each in assay buffer. The UBAN-captured biosensors were then submerged in wells containing different concentrations of mono ubiquitin (Millipore Sigma, U6253), di-ubiquitin K48-linked chains (Boston Biochem, UC-200B), di-ubiquitin K63-linked chains (Boston Biochem, UC-300B) or linear di-ubiquitin chains (Boston Biochem, UC-700B) for 5 min followed by 5 min of dissociation step in assay buffer. For measuring small molecule binding, GST-UBAN-Avitag (human UBAN), GST-Ubv-A-Avitag or GST-Avitag were expressed as biotinylated fusions in KCM chemocompetent BL21 (DE3) pBirA cells and captured using SAX biosensors for biotinylated proteins in assay buffer. Sensor sets were blocked with a solution of 10 mg/ml biocytin for 5 min at 25°C. Binding of compound samples (final concentration 100 μM, 5% DMSO) to coated reference sensors was measured over 5 min followed by a 5 min dissociation step. A negative control of 5% DMSO was also used.

### STD-NMR

For STD experiments the purified $^{15}$N-labelled human NEMO UBAN domain was lyophilized and resuspended in equal amounts of $D_2O$. All compounds tested were dissolved in d6-DMSO to a final concentration of 20 mM. The protein buffer used for all NMR experiments was 50 mM sodium phosphate (pH7.0) containing 50 mM NaCl. The final concentration of the samples contained 1 mM compound, 5% d6-DMSO, 95% $D_2O$ in a final volume of 550 μL. After recording a reference 1D $^1$H excitation sculpting spectrum, $^{15}$N NEMO UBAN was added to a final concentration of 10 μM. All samples were measured on a Bruker Avance III spectrometer at 950 Mhz proton frequency, equipped with a $^1$H, $^{15}$N, $^{13}$C cryogenic triple resonance probe (TCI). Pulse programs were downloaded from the Bruker database and adjusted for the 950 MHz Bruker Avance III spectrometer (Gossert and Jahnke, 2016). In order to suppress the residual water resonances, the excitation sculpting method was used in all measurements. Frequencies for ON and OFF irradiation were set at +0.7 and −30 ppm saturation for 2 s using a 50-ms Gaussian pulse train (40 μW) truncated at 1% with a 50 ms spin-lock to suppress protein signals (CDCA: relaxation delay = 3 s and acquisition time = 1 s). The number of scans was adjusted for the different experiments.

### NanoBiT Assays

NanoBiT® PPI MCS Starter System (Promega, N2014) was utilized for generation of assay vectors as described in Table S1. NanoBiT assays were performed by co-transfection of derivatives of NanoBiT vectors into the HEK293T cell line in a 96-well plate format using Genejuice Transfection Reagent (Millipore Sigma, 70967) according to manufacturer's instructions. The activity of complemented nanoluciferase was measured according to manufacturer's instructions using Nano-Glo® Live Cell Assay System (Promega, N2012) and Synergy™ plate reader (BioTek Instruments).

### Compound Preparation

All test compounds, including Aloe Emodin reference tool inhibitor (Millipore Sigma, 93938) and TPCA-1 (Millipore Sigma, T1452), were solubilized in 100% (v/v) DMSO to 10 mM. For high throughput screening, compounds were acoustically dispensed using an Echo™ 550 Liquid Handler (Labcyte) into wells of white 384-well tissue culture–treated microplates (Greiner Bio-One,781073) containing cells and media. All single-concentration screening was performed at a final concentration of 0.5% (v/v) DMSO maximum control, 50 μM Aloe Emodin reference control and test compound concentration of 10 μM. The chemical compound library was purchased from ENAMINE. "HTS" and "Advanced" collections (together comprising ~200,000 compounds) were used for a subset selection. The library used in this study fulfills the industrial standards applied for drug-like library design: Lipinski rule of 5, Veber's rule and MedChem filters. The screened library is a subset of the above described and has been selected by diversity criteria assuring that its 14,784 compounds cover the same range of properties like LogP, hydrogen bond donor, hydrogen bond acceptor, number of rings fraction of tretrahedral carbon within the structure, while maximizing their diversity as expressed by Tanimoto distance calculated on MACCs fingerprints. Compounds are provided on a reasonable request as dry powders, dry films or DMSO solution after a quality control by 1H NMR and/or HPLC/MS with 90%+ purity.

### Compound Cluster Analysis

For compound cluster analysis selected compound structures from the screened library were imported in a KNIME workflow and coded with MACCS Keys (Durant et al., 2002) as implemented through RDKit nodes. Distance matrix calculation was performed and Tanimoto distance used to the subsequent complete linkage cluster analysis was also conducted in KNIME v.3.7.1 (Salim et al., 2003). Compound CIDs of the top three hits:

| Compound Name: | Compound CID: |
|---|---|
| T-10333 | 60532241 |
| T-10334 | 47050994 |
| T-10336 | 75467915 |

### High Throughput Cellular NanoBiT Screen

HEK293T cells were seeded in 15 cm petri dishes (Sarstedt 82.1184.500) 4.15E+6 cells/petri dish and incubated 24 hours at 37°C and 5% $CO_2$. Cells were transfected with NanoBiT constructs (expressing SmBiT fusion to the human UBAN domain and LgBiT fusion to Ubv-A) in heat inactivated, serum reduced (1 %) media and incubated for 3 hours. After harvesting of transfected cells using cell scraper and centrifugation for 3 min at 200xg cells were resuspended and dispensed using 20,000 cells/well into 384-well plates in 20 μL serum reduced media using the Multidrop Dispenser (Thermo Fisher Scientific). Following 20-hour incubation, compounds were dispensed at 10 μM final concentration and nanoluciferase activity was determined four hours after compound addition and incubation at 37°C and 5% $CO_2$. The response for each individual test compound was quantified after equilibration of the assay plate at room temperature using 20 μL of the Nano-Glo® Live Cell Assay System (Promega, N2012) according to manufacturer's instructions, measured using Envision® plate reader (Perkin Elmer) and depicted as percent inhibition relative to the reference Aloe Emodin inhibitor added at 50 μM final concentration.

### Cell Viability Assay

The effect of compounds on cell viability was studied by a resazurin-based assay using the PrestoBlue™ Cell Viability Reagent (ThermoFisher Scientific, A13261). The experiments were performed similarly as described previously (Boncler et al., 2014; García-Fernández et al., 2017). In brief, HeLa, HEK293T and U2OS cells were seeded in 96-well plates at a concentration of 3.0 x$10^3$ cells/well. After 24 hours incubation at 37°C under controlled conditions, cells were then treated with the compounds at different concentrations ranging from 0 to 200 μM. Cisplatin (cis-diaminedichloroplatinum (II) or CDDP) and the IKKβ kinase inhibitor TPCA-1 were used as reference compounds. After 24 or 72 hours of treatment, aliquots of 20 μl of the PrestoBlue™ Cell Viability Reagent solution were added to each well. After 1 hour incubation with the reagent, the fluorescence emission (λexc=560 nm and λem=590 nm) of each well was measured using a TECAN infinite 200 PRO fluorescence microplate reader. The cytotoxic effect of the different compounds was determined by calculating the half maximal inhibitory concentrations ($IC_{50}$) against the four different cell lines tested. In all the cases, the experiments were performed at least in triplicate.

## QUANTIFICATION AND STATISTICAL ANALYSIS

Ordinary one-way ANOVA multiple comparison was used in Figures 2F, 3E–3H, 4B, and 4C. Multiple comparison corrections were made using the Tukey method with family-wise significance and confidence level of 0.05. Two-tailed unpaired parametric t-test with 95 % confidence level was used in Figure 3D. Outliers were removed using ROUT method (Q = 1 %) where indicated. Line graphs and associated data points represent means of data; error bars represent either standard deviation from mean or standard deviation as indicated in the figure legends. N denotes biological replicates, unless stated otherwise in figure legends. GraphPad Prism 8 software was used for data analysis and representation. P-values: *<0.05, **<0.01, ***<0.001, ****<0.0001.